

Hydrodynamic modeling of the deconfinement phase transition in heavy-ion collisions in the NICA–FAIR energy domain

A. V. Merdeev

National Research Center Kurchatov Institute, 123182 Moscow, Russia

L. M. Satarov and I. N. Mishustin

Frankfurt Institute for Advanced Studies, D–60438 Frankfurt am Main, Germany and National Research Center Kurchatov Institute, 123182 Moscow, Russia

(Received 22 March 2011; published 29 July 2011)

We use $(3 + 1)$ dimensional ideal hydrodynamics to describe the space-time evolution of strongly interacting matter created in Au + Au and Pb + Pb collisions. The model is applied for the domain of bombarding energies 1–160 GeV/nucleon which includes future NICA (Dubna) and FAIR (Darmstadt) experiments. Two equations of state are used, the first one corresponding to resonance hadron gas and the second one including the deconfinement phase transition. The initial state is represented by two Lorentz-boosted nuclei. Dynamic trajectories of matter in the central box of the system are analyzed. They can be well represented by a fast shock-wave compression followed by a relatively slow isentropic expansion. The parameters of collective flows and hadronic spectra are calculated under assumption of the isochronous freeze-out. It is shown that the deconfinement phase transition leads to broadening of proton rapidity distributions, increase of elliptic flows, and formation of the directed antiproton flow in the central rapidity region. These effects are most pronounced at bombarding energies around 10 GeV/nucleon, when the system spends the longest time in the mixed phase. From the comparison with three-fluid calculations we conclude that the transparency effects are not so important in central collisions at NICA–FAIR energies (below 30 GeV/nucleon).

DOI: [10.1103/PhysRevC.84.014907](https://doi.org/10.1103/PhysRevC.84.014907)

PACS number(s): 24.10.Nz, 25.75.Ld, 25.75.Nq

I. INTRODUCTION

Relativistic hydrodynamics is a very powerful tool to study high-energy nuclear collisions. Especially useful is its sensitivity to the “equation of state” (EoS) of strongly interacting matter and, in particular, to its phase diagram. In fact, extracting this EoS is the main goal of heavy-ion experiments. Theoretical studies of the EoS are still not very conclusive. First-principle QCD calculations on the lattice [1,2] give reliable results only at small baryon chemical potentials. In this case a crossover transition from hadronic to quark-gluon degrees of freedom is predicted at temperatures $T \sim 170$ MeV. Some signatures of a baryon-free quark-gluon plasma with low viscosity have been already found [3] in Relativistic Heavy Ion Collider (RHIC) experiments with c.m. bombarding energies $\sqrt{s_{NN}} = 60 - 200$ GeV. These signatures may be even stronger at Large Hadron Collider (LHC) energies ($\sqrt{s_{NN}} \sim 5$ TeV). On the other hand, many phenomenological models predict that a strong first-order phase transition may occur in compressed baryon-rich matter [4–6]. Presumably, such matter is created at lower energies available at the Super Proton Synchrotron (SPS) and the Alternating Gradient Synchrotron (AGS). A more detailed data should be obtained in the low-energy runs at RHIC [7] as well as in future NICA [8] and FAIR [9] experiments.

A large amount of experimental data for nuclear collisions at AGS, SPS, and RHIC energies have been successfully described by different versions of the hydrodynamic model. The first model of this kind was proposed by Landau more than 50 years ago [10]. Unless stated otherwise, below we are

dealing with perfect fluids, i.e., we neglect possible dissipative terms associated with viscosity, heat conductivity, as well as chemical nonequilibrium effects. In other words, it is assumed that deviations from local equilibrium are small, starting from the early stages of a nuclear collision. One can roughly divide the existing versions of ideal hydrodynamics into two classes. The first class includes the models which apply fluid dynamic simulations from the very beginning, i.e., starting from cold equilibrium nuclei. The attractive feature of such an approach is that no additional parameters are needed to characterize the initial state of the reaction. The models of the second class introduce an excited and compressed initial state — a locally equilibrated “fireball.” It is believed that such a fireball is formed at an early nonequilibrium stage of the collision. The disadvantage of this approach is the large freedom in choosing geometrical and fluid-dynamic parameters of the initial state. Due to this reason the predictive power of second-class models is greatly reduced, especially when studying the sensitivity of the results to the EoS. Until now many versions of the fireball-based hydrodynamic model were developed, ranging from simplified $(1+1)$ - [11–16] and $(2+1)$ -dimensional models [13,17–20] to more sophisticated $(3+1)$ -dimensional ones [21–27]. Recent calculations with inclusion of dissipative terms [28,29] show that data at RHIC energies can be reproduced with rather low viscosity coefficients.

Historically, early three-dimensional (3D) models of relativistic nuclear collisions [30–35] used cold Lorentz-contracted nuclei in the initial state. It is believed that such models are good enough up to bombarding energies of about

10 GeV/nucleon. Due to the projectile-target transparency, they become less and less justified with increasing bombarding energy. To take into account this effect, generalized multifluid models have been constructed in Refs. [36–41]. The most important ingredients of such models, the interfluid coupling terms, are rather uncertain and are usually parameterized phenomenologically.

It is clear that a hydrodynamic approach cannot be directly applied to late stages of a heavy-ion reaction when binary collisions of particles become too rare to maintain the local thermodynamic equilibrium. A standard way [10] to circumvent this difficulty is to introduce a so-called “freeze-out” criterion to stop the hydrodynamic description. Often it is postulated that collisionless expansion of particles starts at some isothermal hypersurface [42]. Unfortunately, this approximation is rather crude [43] and even in contradiction with experimental data (see, e.g., [44]). A more consistent procedure has been suggested [18,20,45–47] within a hybrid “hydro-cascade” model. In this scheme hydrodynamics is used for generating coordinates and momenta of hadrons at some intermediate stage of the reaction. These characteristics are used for transport simulations of later stages.

Below we formulate a version of the ideal (3+1)-dimensional hydrodynamics suitable for the domain of AGS, NICA, FAIR, and SPS energies. This model belongs to the first class and uses a new EoS [48] with the deconfinement and liquid-gas phase transitions. In our calculations we perform a detailed analysis of the dynamics of nuclear collisions at various energies, giving particular attention to macroscopic characteristics, i.e., collective flows, lifetime, and volume of quark-gluon and mixed phases. It is shown that maximal energy and baryon densities predicted by our fluid-dynamics simulations agree well with one-dimensional (1D) shock-wave calculations. A special analysis is carried out to evaluate the importance of transparency effects. This is made by comparing our results with predictions of the three-fluid model of Ref. [41]. To calculate momentum spectra as well as directed and elliptic flows of secondary particles, we apply an approximation of isochronous freeze-out. In these calculations we investigate the sensitivity of observables to the finite size of hadrons by introducing excluded volume corrections.

The paper is organized as follows: our hydrodynamic model is formulated in Sec. II. The results of numerical calculations for central Au + Au collisions at FAIR and SPS energies are given in Sec. III. Here we also compare the predictions of the one- and three-fluid models. In Sec. IV we discuss a space-time picture of noncentral Au + Au collisions. Particle spectra and parameters of transverse collective flows are considered in Secs. V and VI. Our conclusions are presented in Sec. VII.

II. FORMULATION OF THE MODEL

A. Equations of ideal fluid dynamics

Below we study the evolution of highly excited, and possibly deconfined, strongly interacting matter produced in ultrarelativistic heavy-ion collisions. It is assumed that this evolution can be described by the equations of ideal relativistic hydrodynamics [49]. These equations represent local

conservation laws of the four-momentum and baryon charge

$$\partial_\nu T^{\mu\nu} = 0, \quad (1)$$

$$\partial_\mu N^\mu = 0. \quad (2)$$

In the limit of small dissipation the baryon four-current N^μ and the energy-momentum tensor $T^{\mu\nu}$ can be expressed as ($\hbar = c = 1$)

$$N^\mu = n u^\mu, \quad (3)$$

$$T^{\mu\nu} = (\varepsilon + P) u^\mu u^\nu - P g^{\mu\nu}, \quad (4)$$

where ε , n , and P are the rest-frame energy density, the net baryon density, and pressure of the fluid, $u^\mu = \gamma(1, \mathbf{v})^\mu$ is its collective four-velocity, $\gamma = (1 - \mathbf{v}^2)^{-1/2}$, and $g^{\mu\nu} = \text{diag}(+, -, -, -)$ is the metric tensor. Here and below we denote by \mathbf{v} the fluid three-velocity.

One can rewrite Eqs. (1) and (2) in Cartesian coordinates (t, \mathbf{r}) as follows:

$$\partial_t E + \nabla(\mathbf{v}E) = -\nabla(\mathbf{v}P), \quad (5)$$

$$\partial_t \mathbf{M} + \nabla(\mathbf{v}\mathbf{M}) = -\nabla P, \quad (6)$$

$$\partial_t N + \nabla(\mathbf{v}N) = 0, \quad (7)$$

where $E = T^{00}$, $M^i = T^{0i}$, and $N = N^0$ are the energy density, the three-momentum density, and the baryon density in the laboratory frame.

The relations between hydrodynamic variables in the laboratory and local rest frames can be written as

$$E = \gamma^2(\varepsilon + v^2 P), \quad (8)$$

$$\mathbf{M} = \gamma^2(\varepsilon + P) \mathbf{v}, \quad (9)$$

$$N = \gamma n. \quad (10)$$

To solve Eqs. (5)–(10) it is necessary to specify the EoS $P = P(n, \varepsilon)$ of the fluid and initial conditions.

B. Equation of state

In our calculations we use the EoS of strongly interacting matter with the first-order deconfinement phase transition (EoS-PT) [48]. The hadronic phase (HP) is described as the hadron resonance gas with inclusion of known hadrons with masses up to 2 GeV. Finite size effects are taken into account by introducing the excluded volume corrections. The same excluded volume parameter $v_e = 1 \text{ fm}^3$ is used for all hadronic species. A Skyrme-like mean field for baryons,

$$U(n) = -\alpha n + \beta n^{7/6}, \quad (11)$$

is added to guarantee that the hadronic matter has a correct saturation point and a liquid-gas phase transition.¹ The deconfined quark-gluon phase (QGP) is described by the bag model EoS with lowest-order perturbative corrections. The phase transition boundaries and characteristics of the mixed phase (MP) are found by using the Gibbs conditions with the

¹In this paper we do not study effects connected with the liquid-gas fragmentation of relatively cold hadronic matter. Below, when speaking about the phase transition, we have in mind the deconfinement-hadronization transition.

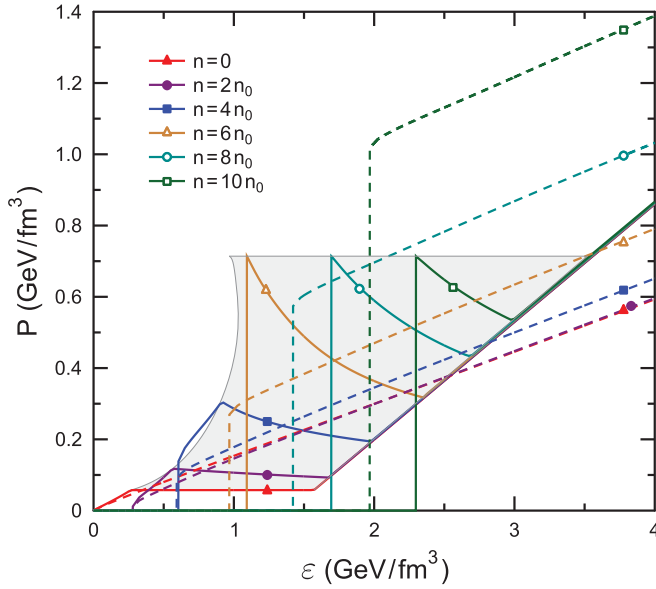


FIG. 1. (Color online) Pressure as a function of energy density at different baryon densities, scaled by saturation nuclear density $n_0 = 0.15 \text{ fm}^{-3}$. Solid and dashed lines correspond to EoS-PT and EoS-HG, respectively. The MP region of the deconfinement phase transition is shown by shading.

strangeness neutrality constraint (for details, see Ref. [48]). The domains of MP states in different thermodynamic variables are shown in Figs. 1, 2, 6, 7, 9, and 10. To probe sensitivity to the EoS, we have also performed calculations with the EoS of ideal hadron gas (EoS-HG). In this case we disregard the excluded volume effects assuming that $v_e = 0$.² To provide stability of initial nuclei, we also introduce the Skyrme-like mean field. The parameters of EoS-PT and EoS-HG are given in [48].

The graphic representation of $P(n, \varepsilon)$ for both EoSs is given in Figs. 1 and 2.³ One can see that values of pressure predicted by these two EoSs significantly differ at large enough ε and n . Important information about the dynamics of matter in the heavy-ion collision can be drawn from Fig. 2, which shows adiabatic trajectories, i.e., lines of constant entropy per baryon, $\sigma = s/n$, where s is the entropy density. As is well known [49], this quantity is conserved along the trajectories of fluid elements in the ideal hydrodynamics (in the absence of shock waves). Our calculations show that in central heavy-ion collisions, larger values of σ are achieved at larger bombarding energies E_{lab} . The slopes of adiabates in Fig. 2 give the sound velocities squared [49]:

$$c_s^2 = \left(\frac{\partial P}{\partial \varepsilon} \right)_\sigma. \quad (12)$$

From Fig. 2 one can see that c_s reaches minimal values (the “softest points”) in the MP region. This should essentially

² As shown in Ref. [48], the realistic phase diagram of strongly interacting matter is possible only with introducing finite sizes of hadrons, i.e., at $v_e \neq 0$.

³ Note that jumps of pressure curves in Fig. 1 correspond to the zero temperature boundary of physical states in the $n - \varepsilon$ plane.

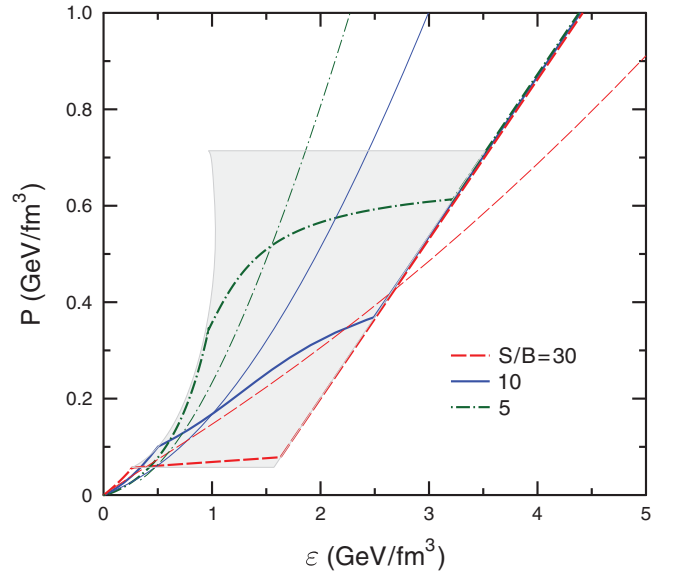


FIG. 2. (Color online) Adiabatic trajectories in the $\varepsilon - P$ plane. Thick and thin lines correspond to EoS-PT and EoS-HG, respectively. Shading shows the MP region of the deconfinement phase transition.

influence the expansion dynamics. Indeed, an instantaneous acceleration of a fluid element is proportional to the gradient of pressure $\nabla P = c_s^2 \nabla \varepsilon$. At given $\nabla \varepsilon$ one may expect smaller accelerations of matter for “softer” EoSs, which have smaller values of sound velocity. As one can see from Fig. 2, the EoS-PT is softer than the EoS-HG only in the right side of the MP domain. In other regions of thermodynamic parameters the EoS-PT has sound velocities of the same order or even larger than those in the EoS-HG. Such a situation may occur in the MP region for intermediate values of specific entropy, e.g., at $S/B = 5$ in Fig. 2. This anomaly is expected in the NICA-FAIR energy domain, where our calculations predict a nonmonotonous behavior of collective flows and particle spectra as functions of bombarding energy (see below).

C. Initial conditions

We start our hydrodynamic simulation from the stage when two cold nuclei approach each other. Unless stated otherwise, we consider collisions of gold nuclei ($Z = 79$, $A = 197$) which have the Woods-Saxon density distribution in their rest frame,

$$n(\mathbf{r}, t = 0) = \frac{n_0}{1 + \exp\left(\frac{|\mathbf{r}| - R_0}{a}\right)}, \quad (13)$$

with the parameters $n_0 = 0.15 \text{ fm}^{-3}$, $a = 0.5 \text{ fm}$, $R_0 = 6.7 \text{ fm}$. We assume that the rest frame initial energy density of each nucleus, $\varepsilon(\mathbf{r}, t = 0)$, is given by the right-hand side of (13) with the replacement of n_0 by $\varepsilon_0 = \mu_0 n_0$, where $\mu_0 = 0.923 \text{ GeV}$ is the baryon chemical potential of equilibrium nuclear matter. Due to the stabilizing effect of the Skyrme-like mean field, the initial nuclei may stay in equilibrium with vacuum at $P = 0$. They propagate without distortion until their density distributions essentially overlap.

The c.m. collective velocity of nuclei at $t = 0$ is taken as $v_0 = \sqrt{E_{\text{lab}}/(2m_N + E_{\text{lab}})}$, where $m_N = 0.939$ GeV is the nucleon mass and E_{lab} is the projectile bombarding energy (per nucleon) in the laboratory frame. Below the beam axis is denoted by z and the x axis is chosen along the impact parameter vector \mathbf{b} . In this case the reaction and transverse planes correspond to $y = 0$ and $z = 0$, respectively. The initial longitudinal distance between the target and projectile centers in the c.m. frame is chosen as

$$z_t(0) - z_p(0) = 2(R_0 + 6.9a)/\gamma_0, \quad (14)$$

where $\gamma_0 = (1 - v_0^2)^{-1/2}$ is the Lorentz factor of colliding nuclei.⁴

D. Numerical scheme

The numerical solution of fluid-dynamic equations (5)–(7) was obtained by using the flux-corrected transport algorithm SHASTA [50,51]. All calculations are performed in the c.m. frame. Unless otherwise stated, we use a cubic Eulerian grid with the cell size $\Delta x = 0.1$ fm along each coordinate direction. Typically we take the numbers of grid points equal to $500 \times 300 \times 400$ in x, y, z directions and choose the time step $\Delta t = 0.01$ fm/c. In our simulations we use linear interpolations of tables $P(n, \epsilon)$ calculated with fixed steps in n and ϵ . We have checked that our numerical scheme conserves the total baryon number and energy with relative accuracy better than 1%. The program code explicitly uses the symmetry of the collision process with respect to the reaction plane $y = 0$. This reduces the computational memory by a factor of two. A typical run for the 10 A GeV Au + Au collision at $b = 7$ fm requires about 6 Gb of memory and approximately 6 hours of CPU time on a machine with the 2.1 GHz AMD Opteron processor.

Below we often analyze time evolution of fluid-dynamic quantities averaged over a “central box” around the symmetry point $x = y = z = 0$. As a rule, we use a box with dimensions⁵

$$|x|, |y|, \gamma_0|z| < 1 \text{ fm}. \quad (15)$$

For comparison Fig. 3 shows the time dependence of the baryon density in the central grid cell and in the central box for the case of a central Au + Au collision at $E_{\text{lab}} = 10$ GeV/nucleon. One can see that using rough grids leads to oscillations of the energy density which are of numerical origin. They are especially noticeable at early stages of a collision when a shocklike compressed zone is formed (see Sec. III B). The spatial profile of the compressed zone is determined by the Woods-Saxon density distributions of the colliding nuclei and the width of the shock front. The latter is related to the numerical viscosity associated with a finite cell size Δx . This explains the different slopes of density curves in Fig. 3. Assuming that the numerical calculation with $\Delta x =$

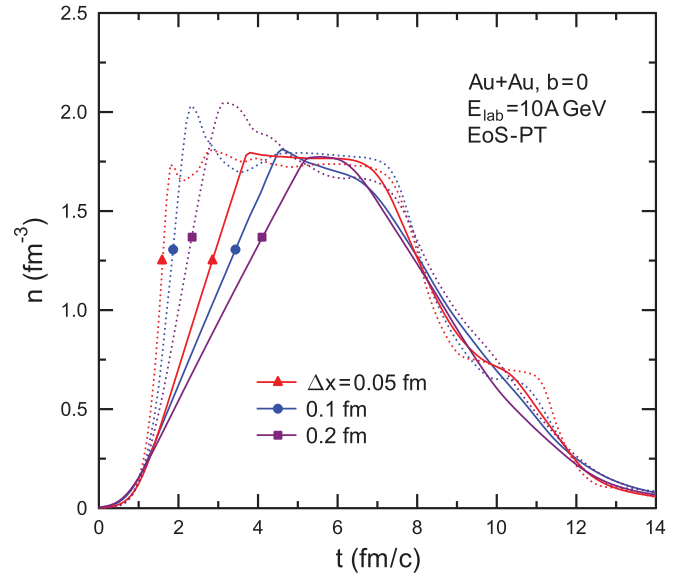


FIG. 3. (Color online) The rest-frame baryon density n as a function of time in a central ($b = 0$) Au + Au collision at $E_{\text{lab}} = 10$ GeV/nucleon. Dotted lines show density in a central cell, while solid ones represent density values averaged over the central box. Different colors correspond to calculations with different Δx . All results are obtained for EoS-PT.

0.05 fm gives a nearly exact solution of ideal hydrodynamics in a continuum limit, we conclude that visible deviations at $\Delta x = 0.1$ fm and especially at $\Delta x = 0.2$ fm are caused by the numerical viscosity. Most of our calculations are performed with $\Delta x = 0.1$ fm, when the effect of numerical viscosity is small, at the level of a few percent in thermodynamic quantities.

E. Particle spectra and parameters of collective flows

To calculate hadronic momentum distributions we apply the approximation of instantaneous freeze-out: it is assumed that a sudden transition from the local equilibrium to collisionless propagation of particles takes place at some space-time hypersurface σ_μ .⁶ Within this approximation one can use the standard Cooper-Frye formula [42] for the invariant momentum distribution of the hadronic species i ,

$$E \frac{d^3 N_i}{d^3 p} = \frac{d^3 N_i}{dy d^2 p_T} = \frac{g_i}{(2\pi)^3} \int d\sigma_\mu p^\mu \left\{ \exp \left(\frac{p_\nu u^\nu - \mu_i}{T} \right) \pm 1 \right\}^{-1}, \quad (16)$$

where $p^\mu = (E, \mathbf{p})^\mu$ is the four-momentum of the particle, y and \mathbf{p}_T are, respectively, its longitudinal rapidity and

⁴From Eqs. (13) and (14) one can see that in the case of a central collision the rest frame density of each nucleus at $x = y = z = ct = 0$ equals approximately $10^{-3} n_0$.

⁵At $E_{\text{lab}} \geq 80$ GeV/nucleon we use energy-independent sizes of the central box: $|x|, |y| < 1$ fm, $|z| < 0.2$ fm. In Fig. 8 a larger box is used with sizes increased by a factor of 2 as compared to Eq. (15).

⁶It is also postulated that the presence of already-frozen fluid elements does not significantly influence the dynamics of remaining parts of the system.

transverse momentum, T denotes the local temperature, and g_i is the statistical weight of the hadron species i . Plus and minus in (16) correspond, respectively, to fermions and bosons. Using conditions of chemical equilibrium, one can express the particle's chemical potential μ_i through the baryon (μ) and strange (μ_S) chemical potentials as follows [48,52]:

$$\mu_i = B_i \mu + S_i \mu_S, \quad (17)$$

where B_i and S_i are, respectively, the baryon and strangeness number of species i .

In calculating spectra of baryons ($B_i = 1$), we take into account the mean-field effects. In this case we use Eqs. (16) and (17) with the replacement of the baryon chemical potential μ by its "kinetic" part $\mu_K = \mu - U(n)$, where $U(n)$ is the mean-field potential introduced in (11). As indicated above, our calculations with the deconfinement phase transition use the EoS with inclusion of finite-volume corrections. In accordance with Refs. [48,53], we introduce these corrections by the replacement $\mu_i \rightarrow \mu_i - v_i P_K$, where P_K is the kinetic part [48] of the total pressure and v_i is the excluded volume of the i th hadron. Unless stated otherwise, particle spectra and collective flows in the case of EoS-PT are calculated by using the parameter $v_i = 1 \text{ fm}^3$ for all hadronic species.

For our qualitative analysis we chose the simplest condition of isochronous freeze-out ($t = t_{\text{fr}} = \text{const}$). Then $d\sigma_\mu = d^3x \delta_{\mu,0}$ and Eq. (16) gives the hadronic momentum distribution at a fixed time t in the c.m. frame. In addition to contributions of "thermal" nucleons and pions, which are calculated directly by using (16), we also take into account resonance decays, e.g., $\Delta \rightarrow N\pi$, $\rho \rightarrow 2\pi$. Below we assume zero widths of resonances and apply the following formula [16] for the spectrum of hadrons i from two-body decays $R \rightarrow i + X$:⁷

$$E \frac{d^3 N_{R \rightarrow i}}{d^3 p} = \frac{b_i}{4\pi q_0} \int d^3 p_R \frac{d^3 N_R}{d^3 p_R} \delta\left(\frac{p p_R}{m_R} - E_0\right). \quad (18)$$

Here m_R and p_R are the mass and four-momentum of the resonance R ($R = \Delta, \rho, \dots$), E_0 and q_0 are the energy and three-momentum of the hadron i in the rest frame of R , and b_i is the branching ratio of the decay channel $R \rightarrow i + X$. Equation (16) is used to calculate spectrum of resonances (in the Boltzmann approximation). All known hadronic resonances with masses up to 2 GeV are taken into account. The statistical weights, branching ratios, and masses of these resonances are taken from [54].

Transverse collective flows of matter created in heavy-ion collisions are rather sensitive to its EoS. Much attention in recent years is given to the parameter of elliptic flow v_2 [55]. The 2+1 fluid-dynamic calculations at SPS and RHIC energies [20,56] show a significant sensitivity of this quantity to the deconfinement phase transition. The elliptic flow of i th

hadrons ($i = \pi, N, \dots$) is usually determined as

$$v_2^{(i)}(y) = \frac{\int d^2 p_T \cos(2\phi) E d^3 N_i / d^3 p}{\int d^2 p_T E d^3 N_i / d^3 p}, \quad (19)$$

where $\phi = \arccos(p_x/p_T)$ is the azimuthal angle of \mathbf{p}_T with respect to the reaction plane. Here $d^3 N_i / d^3 p$ is the momentum distribution of i th hadrons with inclusion of resonance decays. Unfortunately, the elliptic flow is sensitive [46,57,58] not only to the EoS, but also to dissipative and freeze-out effects. Below we also calculate the directed flow parameter $v_1^{(i)}(y)$. It is defined by the right-hand side of (19) with the replacement $\cos(2\phi) \rightarrow \cos\phi$. It is clear that $v_1, v_2 \rightarrow 0$ for purely central collisions ($b \rightarrow 0$).

To discuss qualitatively possible differences between the EoS-PT and EoS-HG at different bombarding energies, below we calculate a so-called momentum anisotropy parameter ϵ_p which characterizes the collective flow asymmetry in the transverse plane. Following Ref. [60] we define this quantity as

$$\epsilon_p = \frac{\int dx dy (T^{xx} - T^{yy})}{\int dx dy (T^{xx} + T^{yy})}, \quad (20)$$

where T^{xx}, T^{yy} are the components of momentum density in the transverse plane $z = 0$.⁸ In Ref. [17] the approximate relation $\epsilon_p \simeq 2v_2^{(\pi)}(0)$ has been obtained from (2+1)-hydrodynamic simulations of Pb + Pb collisions at SPS and RHIC energies.

III. EVOLUTION OF FLUID-DYNAMIC QUANTITIES IN CENTRAL COLLISIONS

A. Comparison of results for EOS-PT and EOS-HG

Below we discuss thermodynamic characteristics of matter created in Au + Au collisions at various bombarding energies. Our goal is to find differences between the results obtained with EoS-HG and EoS-PT. Let us first consider purely central collisions with $b = 0$. Figures 4–9 show the time evolution of the rest frame energy and baryon densities averaged over the central box defined in Sec. II D. One can see that after a rapid initial growth the baryon and energy densities remain practically constant during certain time intervals (depending on the bombarding energy E_{lab}) and only later do they start to decrease. The plateau is explained by running shock waves created at an early stage of the reaction. Within the considered one-fluid approach, the entropy of matter is generated via the shocklike compression mechanism (see the next section)

⁷The decay channels with more than two final hadrons are included approximately. Namely, we consider the decay into $n + 1$ hadrons $R \rightarrow i + h_1 + \dots + h_n$ ($n > 1$) as a reaction $R \rightarrow i + X$, where X is a hadronic cluster with mass equal to the total mass of hadrons h_1, \dots, h_n at rest.

⁸Experimentally one cannot fix longitudinal coordinates of particles in a central slice. Instead, those particles are usually observed whose c.m. rapidities y_i fall in some window $|y_i| < y_*$. In the Bjorken scaling picture, such a window corresponds to an expanding layer $|z_i| < \Delta z = \tanh y_* t$. To take this into account, we also perform calculations using a modified definition of the momentum anisotropy, with additional integration over $|z| < \Delta z$ in the numerator and denominator of (20). This modification is applied only for $t > R/\gamma_0$.

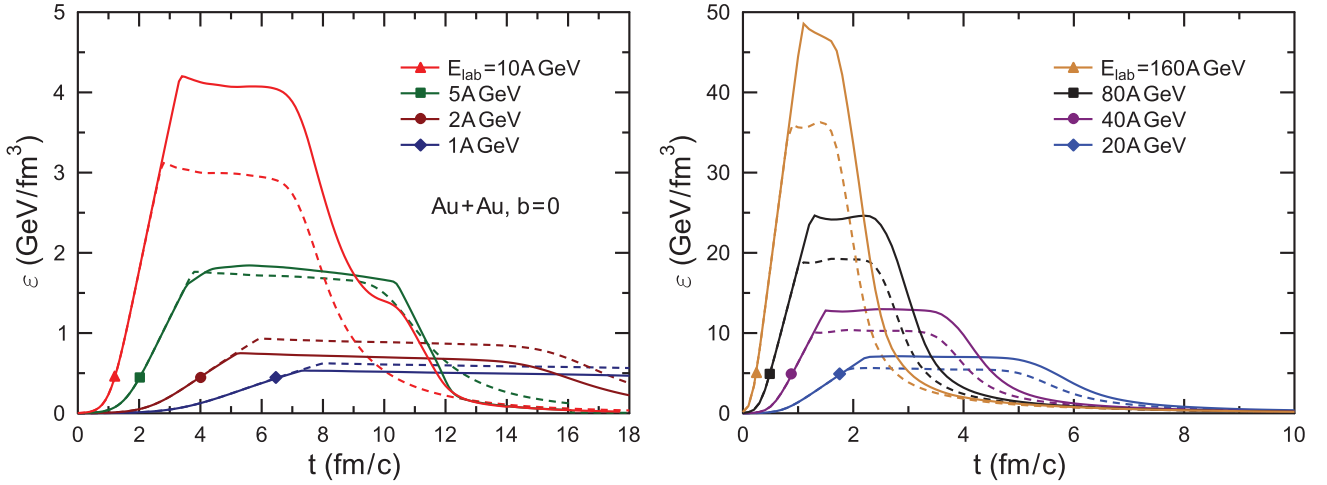


FIG. 4. (Color online) Time evolution of the energy density in the central box of a central Au + Au collision for various bombarding energies. Solid and dashed lines correspond to EoS-PT and EoS-HG, respectively.

which converts the c.m. kinetic energy of projectile and target nucleons into internal energy of stopped matter. The plateaus in Figs. 4 and 5 begin at the moments in time when the shock waves reach the dense central parts of colliding nuclei. Initially these shocks appear at the central point $r = 0$ in the c.m. frame and then propagate outward through the colliding nuclei. Right-end points of the plateaus correspond to the moments when rarefaction waves, propagating from rear sides of nuclei, reach the central point. One can see that at $E_{\text{lab}} \gtrsim 5$ GeV/nucleon, when matter enters MP states, the calculation with the EoS-PT predict larger values of ε and n as compared with the EoS-HG.

B. Simplified picture of matter evolution in a central box

To estimate parameters of states with maximal compression, let us consider a collision of two slabs of cold nuclear matter ($n = n_0$, $T = 0$) moving initially with velocities $\pm v_0$ along the z axis. After the first contact two shock fronts start to

propagate with constant velocities in the positive and negative z directions. Following Ref. [49], from the continuity of T^{0z} , T^{zz} , N^z in the shock front rest frame one gets the relation (so-called Rankine-Hugoniot-Taub adiabat) connecting the baryon (n) and energy (ε) densities of fluid behind the shock front:

$$\varepsilon_0(P + \varepsilon_0)n^2 = \varepsilon(P + \varepsilon)n_0^2, \quad (21)$$

where $\varepsilon_0 = \mu_0 n_0$ is the initial rest-frame energy density of each slab.⁹

In addition, one can write down the equation expressing conservation of energy per baryon at the shock front. In the c.m. frame this equation looks like the stopping condition

$$\varepsilon/n = \gamma_0 \varepsilon_0/n_0, \quad (22)$$

⁹The explicit form of (21) is obtained assuming that the initial pressure $P_0 = P(n_0, \varepsilon_0) = 0$.

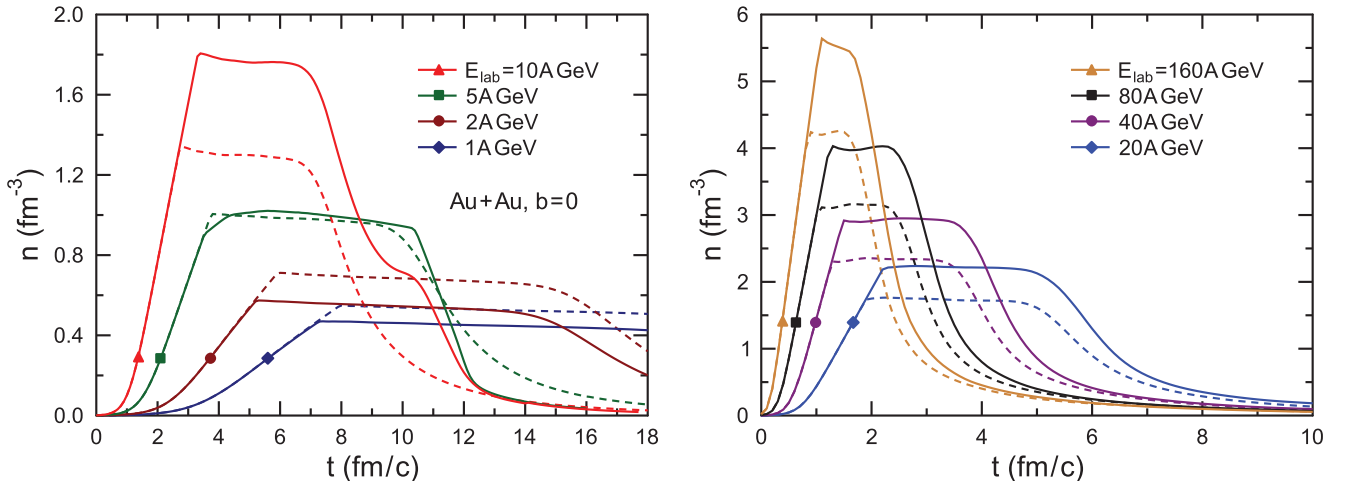


FIG. 5. (Color online) Same as Fig. 4, but for net baryon density.

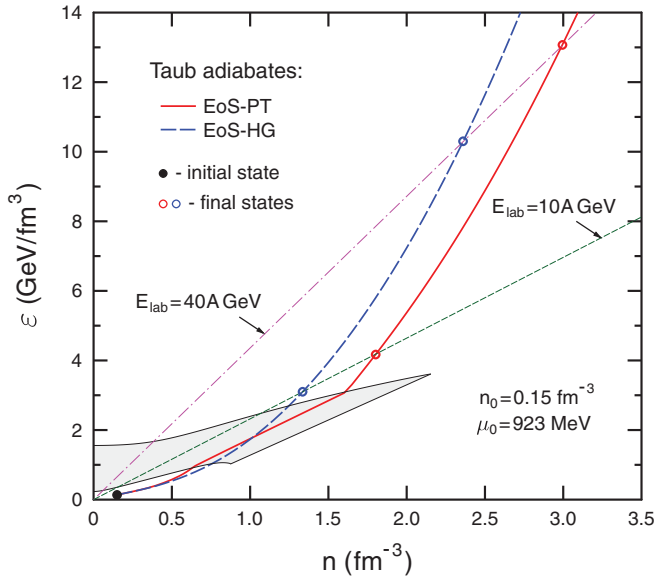


FIG. 6. (Color online) Taub adiabates and parameters of shock waves for collisions of two slabs of normal nuclear matter at $E_{\text{lab}} = 10$ and 40 GeV/nucleon. Thin straight lines represent stopping conditions (22) for these values of bombarding energy. Thick solid and dashed lines are the Taub adiabates (21) for EoS-PT and EoS-HG, respectively. The full dot shows the initial state $n = n_0$, $T = 0$. Open dots represent parameters of compressed zone behind the shock fronts. Shading shows the MP region of the deconfinement phase transition.

where $\gamma_0 = (1 + E_{\text{lab}}/2m_N)^{1/2}$ is the initial Lorentz factor. Graphic solutions of Eqs. (21) and (22) for two EoSs used in this paper are shown in Fig. 6.¹⁰ One can see that at $E_{\text{lab}} \gtrsim 10$ A GeV calculations with the EoS-PT predict noticeably higher maximal values of ε and n as compared with the EoS-HG. This in turn leads to higher collective flows of matter in hydrosimulations with the phase transition. Comparison with parameters of maximal compression in central Au + Au collisions (see Figs. 4 and 5) shows good agreement between the Taub adiabat predictions and fluid-dynamic calculations. Our shock-wave calculations with EoS-PT show that compressed states enter the MP region at $E_{\text{lab}} \simeq 3.7$ A GeV and exit it at $E_{\text{lab}} \simeq 7.2$ A GeV. Therefore, effects of the phase transition become noticeable only at bombarding energies above 4 – 5 GeV/nucleon.¹¹

Decreasing parts of curves in Figs. 4 and 5 correspond to the expansion stage of system evolution in the central box. It can be shown that this expansion proceeds quasiadiabatically, i.e., with nearly constant entropy per baryon σ (small deviations are caused by numerical viscosity and by averaging over

¹⁰For both EoSs considered in this paper we get only a single solution at fixed bombarding energy. More complicated solutions including double shocks, deflagration, and detonation waves were also discussed in the literature (see, e.g., [61–63]).

¹¹According to Figs. 4 and 5, there are some differences between the EoS-PT and EoS-HG calculations at energies $E_{\text{lab}} = 1 - 2$ GeV/nucleon. This is a consequence of excluded volume effects disregarded in the EoS-HG.

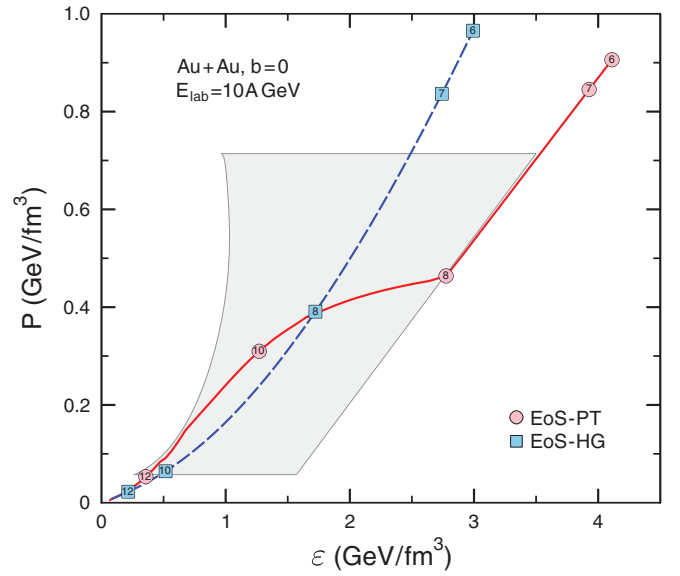


FIG. 7. (Color online) Pressure as a function of energy density in a central box for central Au + Au collisions at $E_{\text{lab}} = 10$ GeV/nucleon. Dashed and solid lines give the results for EoS-HG and EoS-PT, respectively. Numbers in squares and circles denote the values of c.m. time (shown are states at $t > 6$ fm/c only). Shading represents the MP region.

cells in the central box). Figure 7 shows time evolution of thermodynamic parameters in the central box for the case of central Au + Au collisions at $E_{\text{lab}} = 10$ GeV/nucleon. Only late stages of the reaction in the $\varepsilon - P$ plane are considered. Comparison with trajectories in Fig. 2 shows that in the considered case the fluid expansion in the central box proceeds along the adiabat with $\sigma \sim 10$ (for both EoSs). From Figs. 4, 5, and 7 one can see that in the case of the EoS-PT the system expands with some delay as compared with the EoS-HG, i.e., the same values of ε and n are achieved at later times. However, due to differences in pressure, final hadronic states predicted for the EoS-PT and EoS-HG have, generally speaking, different collective velocities.

C. Comparison of one- and three-fluid models

It should be stressed that the results presented above were obtained under the assumption of full mutual stopping of projectile and target matter. Presumably, this approximation should be less justified with raising bombarding energies (see a more detailed discussion in [59]). To estimate the importance of projectile-target transparency effects, we have compared our calculations with the results of the three-fluid model of Ref. [41]. The standard version of this model applies a purely hadronic EoS. In addition, sharp density profiles of initial nuclei are assumed. To make the comparison possible, we performed our calculations with the EoS-HG, choosing a small diffuseness parameter $a = 0.01$ fm [see (13)]. The results of this comparison are presented in Fig. 8. One can see that in the case of central Au + Au collisions the differences between the one- and three-fluid calculations are rather small at $E_{\text{lab}} \lesssim 30$ GeV/nucleon. At larger bombarding energies

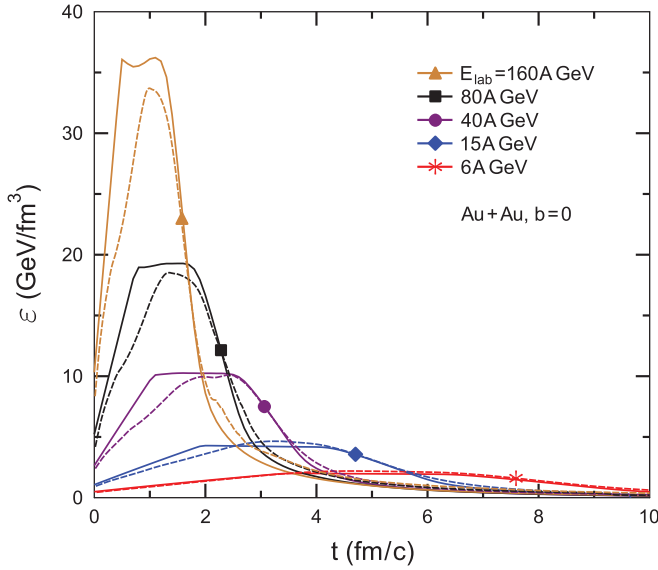


FIG. 8. (Color online) Time evolution of energy density in the central box of central Au + Au collisions with different E_{lab} . Solid lines show our results in the case of EoS-HG and sharp density distributions of initial nuclei. Dashed lines represent three-fluid calculations [64].

maximal values of ε predicted by one-fluid calculations are about 10% larger than in the three-fluid model. In addition, the latter predicts a noticeably slower increase of energy density at the initial stage of the collision. From these results we conclude that transparency effects are not so strong, at least in central Au + Au collisions at FAIR energies and below.

D. Space-time picture of central Au + Au collision

Figures 9 and 10 represent dynamic trajectories of matter (the central box) produced in central Au + Au collisions at different bombarding energies. Shown are results for $n - \varepsilon$ and

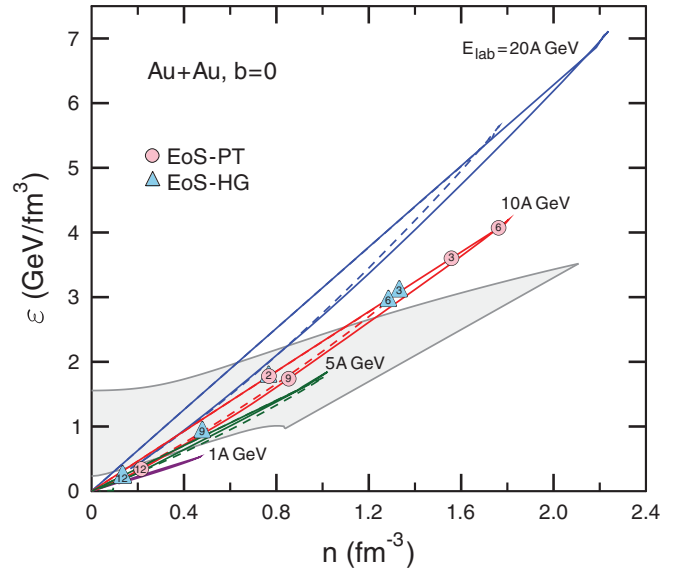


FIG. 9. (Color online) Time evolution of matter in central Au + Au collision at different E_{lab} . Shown are values of energy and baryon densities averaged over the central box. Dashed and solid lines correspond to EoS-HG and EoS-PT, respectively. Numbers in triangles and circles give the c.m. time in fm/c. Shading shows MP region of deconfinement phase transition.

$\mu - T$ planes, respectively. As compared with the EoS-HG, the calculations with the phase transition predict longer lifetimes of states with maximal compression and additional time delays of expansion stages. Especially large differences between two EoSs are visible at intermediate times in the $\mu - T$ plane. The dotted line in Fig. 10 shows the MP region in this plane. As discussed in [65], due to effects of strangeness neutrality, the region of MP states is not a line, as in the case of one conserved charge, but a strip. However, at $v_e \lesssim 1 \text{ fm}^3$ the latter is rather narrow [48] and practically not distinguishable from the dotted line in Fig. 10. The calculations with EoS-PT

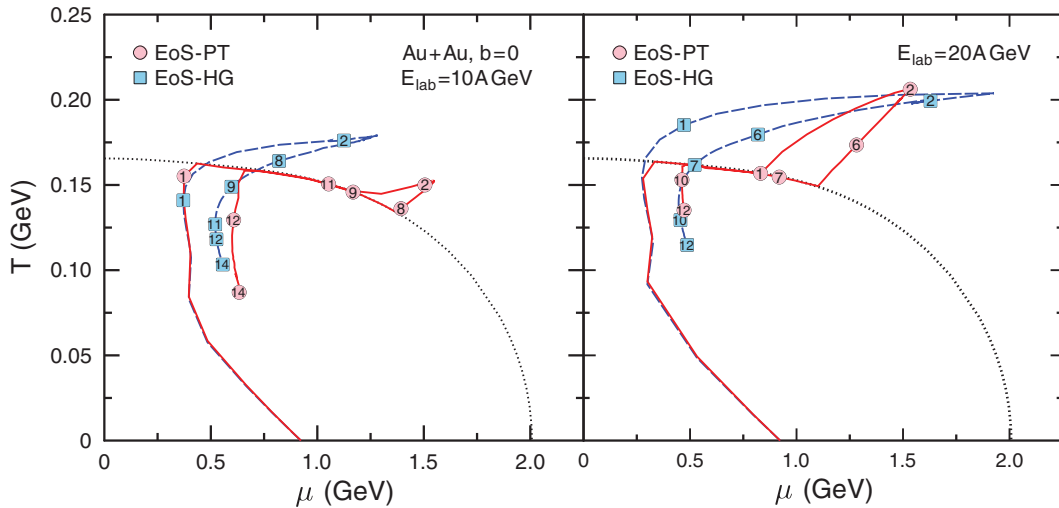


FIG. 10. (Color online) Time evolution of matter (central cell) in the $\mu - T$ plane. Left and right panels correspond to central Au + Au collisions at $E_{\text{lab}} = 10$ and 20 GeV/nucleon , respectively. Dashed (solid) lines show the results for EoS-HG (EoS-PT). Numbers in squares and circles give time values in fm/c.

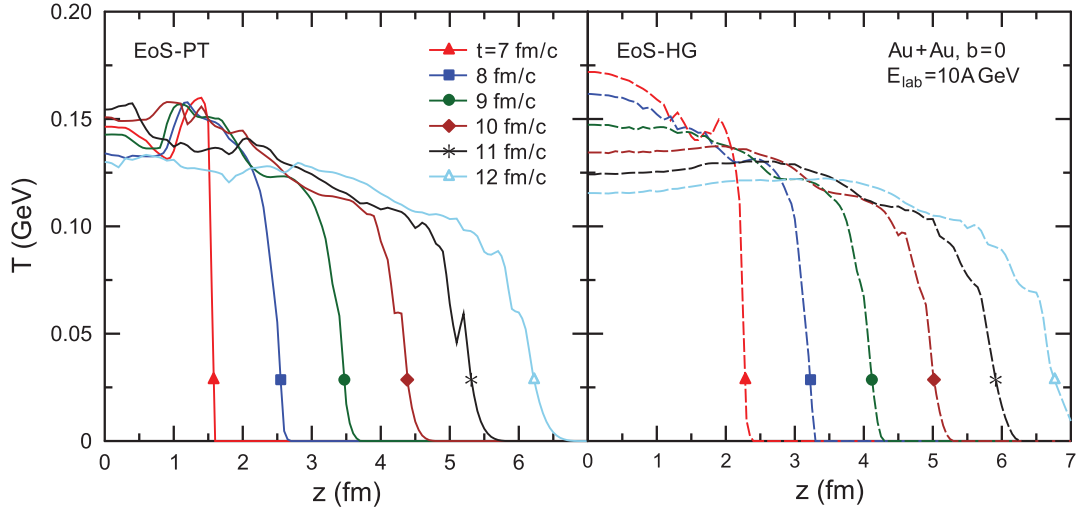


FIG. 11. (Color online) The temperature profiles along the beam axis at different time moments in central 10 A GeV Au + Au collision. The left (right) panel corresponds to EoS-PT (EoS-HG). The results for $z > 0$ only are shown.

predict a zigzag-like behavior of the trajectories in the $\mu - T$ plane with slightly raising temperature in the MP as a function of time. On the other hand, the trajectories do not bend at the MP boundaries in the $n - \varepsilon$ plane. According to Figs. 9 and 10, the largest lifetimes of the MP in central Au + Au collisions, about 4 fm/c, are reached at $E_{\text{lab}} \sim 10$ GeV/nucleon. At lower energies the MP region is traversed only partly, while at higher E_{lab} the produced matter expands too fast.

Figures 11 and 12 show the temperature and pressure profiles as functions of the longitudinal coordinate along the beam axis ($x = y = 0$) for central Au + Au collision at $E_{\text{lab}} = 10$ GeV/nucleon. It is interesting that in the case of EoS-PT the temperature at small $|z|$ changes nonmonotonically in the interval $t = 8 - 12$ fm/c. This follows from a specific behavior of the critical temperature as a function of μ . Indeed, as one can see from Fig. 10, the temperature of MP in a

central slice increases noticeably during the expansion. Such a behavior is explained by the release of latent heat in the hadronizing process. According to Fig. 12, the deconfinement phase transition leads to slower drop of pressure gradients in expanding matter along the beam direction. These gradients are especially large at the MP boundary. This results in strong acceleration of fluid cells during the hadronization processes. As shown below, such acceleration leads to additional broadening of baryon rapidity distribution as compared to a purely hadronic scenario (see Sec. V).

Comparison of spatial distributions of energy density for two EoSs is made in Fig. 13. It represents the contour plots of ε in the reaction plane of a 10 GeV/nucleon central Au + Au collision at $t = 8$ fm/c. Calculation with the EoS-PT shows that at this time the central zone is still in the MP. In this case maximal values of energy density are noticeably higher as compared with the EoS-HG.

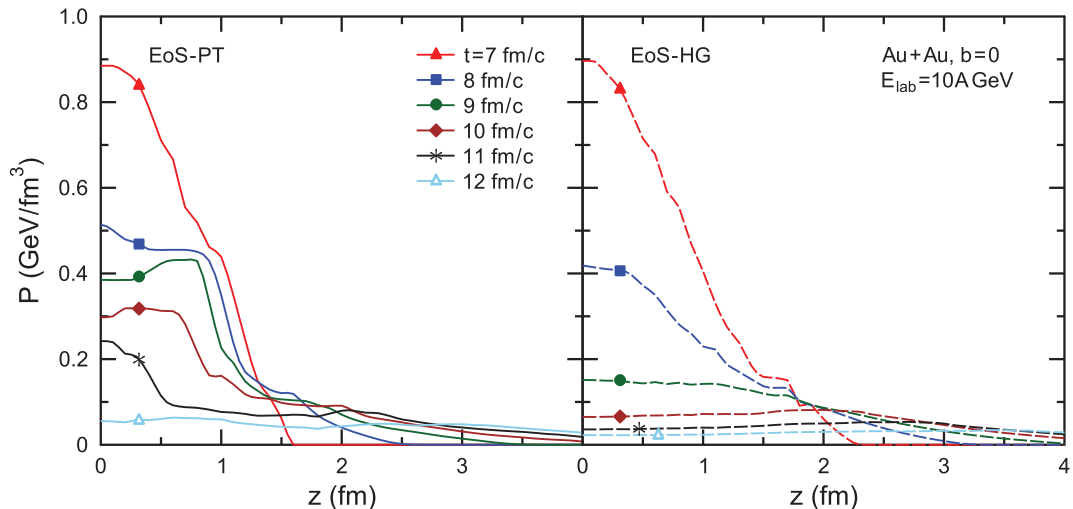


FIG. 12. (Color online) Same as Fig. 11 but for the pressure profiles along the beam axis.

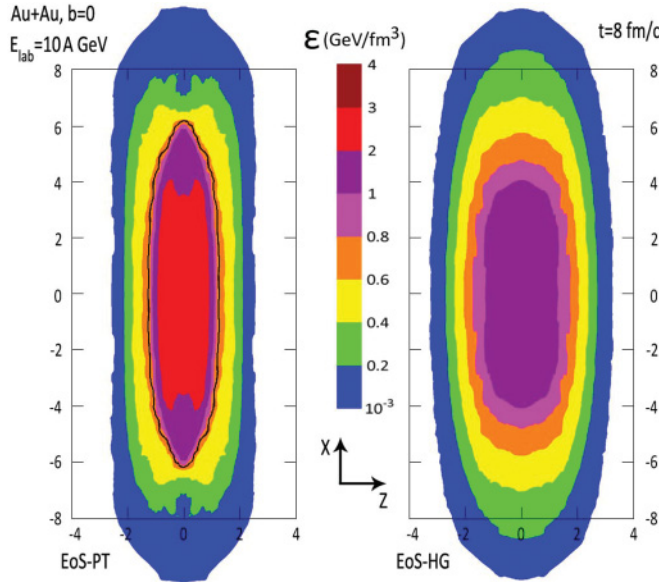


FIG. 13. (Color online) Contours of equal energy densities (in GeV/fm^3) in the reaction ($y = 0$) plane at $t = 8 \text{ fm}/c$ for central 10 A GeV Au + Au collision. The left (right) panel corresponds to EoS-PT (EoS-HG). Numbers near the vertical and horizontal lines show the x and z coordinates in fm. Thick line in the left panel shows the boundary of MP.

IV. MODELING NONCENTRAL COLLISIONS

A. Energy density and collective velocities in Au + Au collisions at $E_{\text{lab}} = 10 \text{ A GeV}$

Let us now consider noncentral collisions. As we see below, especially interesting is the region of bombarding energies, $\sim 10 \text{ GeV}/\text{nucleon}$. At such energies we expect an enhanced sensitivity of collective flow observables and particle spectra to the phase transition. In this section we present results for

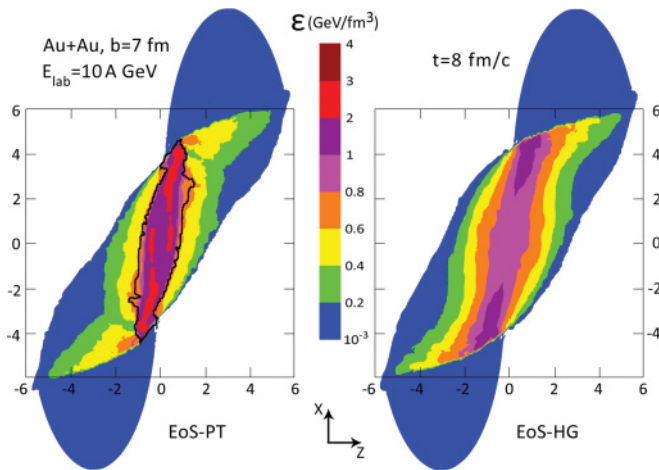


FIG. 14. (Color online) Contours of equal energy densities in the reaction ($y = 0$) plane at $t = 8 \text{ fm}/c$ for 10 A GeV Au + Au collision with $b = 7 \text{ fm}$. The left (right) panel corresponds to EoS-PT (EoS-HG). Numbers near the vertical and horizontal lines show the x and z coordinates in fm. The thick line in the left panel shows the boundary of MP.

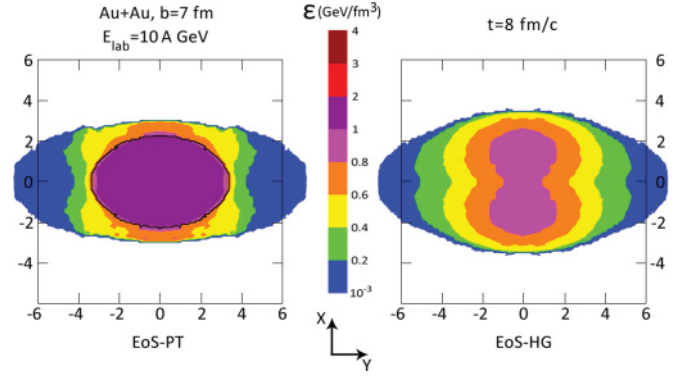


FIG. 15. (Color online) Same as Fig. 14, but for the transverse plane $z = 0$.

10 GeV/nucleon Au + Au collisions with the impact parameter $b = 7 \text{ fm}$.

Figures 14–17 show contour plots of the energy density and three-velocity fields in the reaction ($z - x$) and transverse ($y - x$) planes at $t = 8 \text{ fm}/c$. One can see that in calculation with the EoS-PT, a significant part of the system at this stage is still in the MP.

Figures 16 and 17 represent the collective velocity fields for the same reaction. Blue-colored central regions in these figures correspond to spatial domains with relatively low absolute values of c.m. velocity, $v \lesssim 0.2c$. At the considered time moment, such a region occupies a much larger fraction of space in the calculation with the deconfinement phase transition. According to Figs. 16 and 17, the MP matter is practically at rest in the c.m. frame. On the other hand, pronounced collective flows of hadronic matter are formed in transverse directions. Especially large transverse velocity components appear in the region of geometrical overlap of initial nuclei, at outer edges of the HP. The qualitative structure of the velocity fields may be understood if one takes into account that fluid elements are accelerated mainly along the directions of largest gradients of energy density (see Sec. II B). In particular, this leads to the

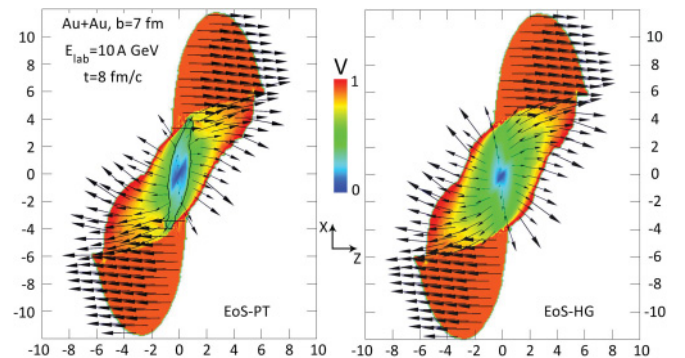


FIG. 16. (Color online) Collective velocities of matter in the reaction plane for midcentral 10 A GeV Au + Au collision ($t = 8 \text{ fm}/c$, $b = 7 \text{ fm}$). Left and right panels correspond to EoS-PT and EoS-HG, respectively. Lengths and directions of arrows represent three-velocity vectors. Numbers show the z and x coordinates in fm. Thick line in the left panel shows the boundary of MP. Vertical color strips characterize three-velocity modules in units of speed of light.

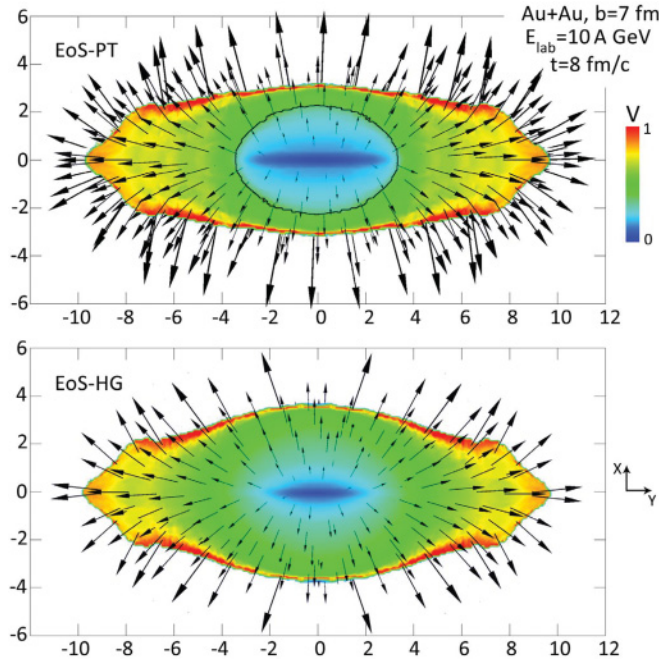


FIG. 17. (Color online) Collective velocities of matter in the transverse plane for 10 A GeV Au + Au collision ($t = 8$ fm/c, $b = 7$ fm). Upper and lower panels correspond to EoS-PT and EoS-HG, respectively. Numbers show the x and y coordinates in fm. Thick line in the upper panel shows the boundary of MP. Vertical color strips characterize three-velocity modules in units of speed of light.

effect of “antiflow,” i.e., to the appearance of fluid elements with opposite signs of v_x and v_z in the reaction plane (see Fig. 16).

According to Fig. 15, at $E_{\text{lab}} \simeq 10$ GeV/nucleon the EoS-PT leads to an essentially different spatial symmetry of the energy-density distribution in the transverse plane as compared with the purely hadronic EoS. On the other hand, calculation with the EoS-PT predicts much larger pressure gradients and

accelerations of matter in the x and y directions. In Fig. 18 we compare the pressure profiles for both EoSs at different times. One can see that in the case of the EoS-PT, especially strong pressure gradients at $t \sim 8$ fm/c are formed in the x direction, at the boundary between the hadronic and mixed phases. This in turn leads to an enhanced momentum anisotropy in the case of EoS-PT as compared with the EoS-HG (see the following section).¹²

B. The momentum anisotropy at different bombarding energies

Here we present the results concerning the momentum anisotropy ϵ_p in (semi)peripheral Au + Au collisions. This quantity has been defined in Eq. (20). Figure 19 represents the time evolution of ϵ_p at different E_{lab} . Thick lines are calculated using the generalized definition of ϵ_p with $y_* = 0.5$ (see footnote 8). By thin lines (for $E_{\text{lab}} = 10$ GeV/nucleon) we also present calculations in the limit $y_* \rightarrow 0$. One can see that in the case with phase transition the simplified formula (20) leads to an unphysical maximum of $\epsilon_p(t)$ at intermediate times. According to Fig. 19, the momentum anisotropy is rather sensitive to EoS in the bombarding energy range $E_{\text{lab}} \lesssim 20$ GeV/nucleon. The asymptotic values of ϵ_p at $E_{\text{lab}} \gtrsim 10$ GeV/nucleon are larger in calculations with the deconfinement phase transition. We think that such a “counterintuitive” result¹³ may be explained by the difference in pressure gradients in the transverse plane. As discussed at the end of the preceding section, they are much larger at intermediate times if the MP is created.

As mentioned in Sec. II E, the freeze-out effects may significantly change the observed values of transverse flows in

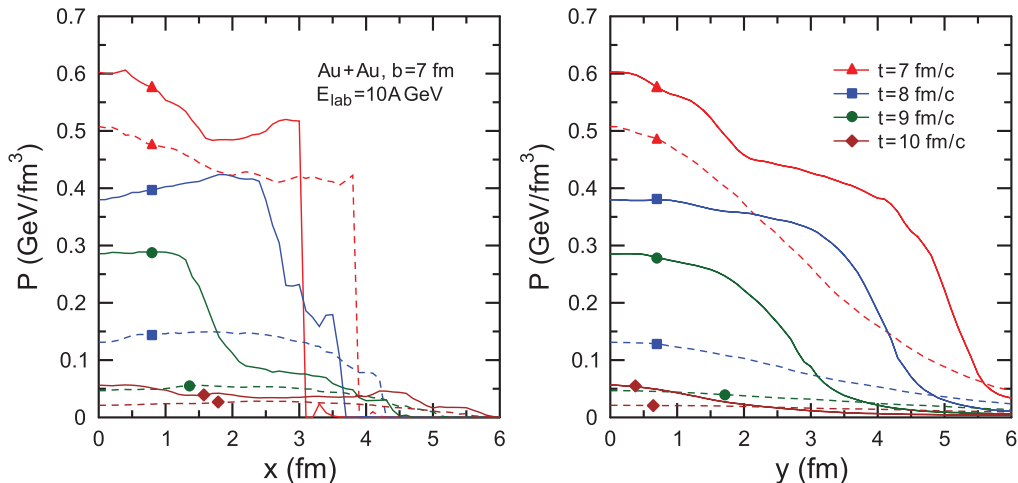


FIG. 18. (Color online) The pressure profiles in 10 A GeV Au + Au collision ($b = 7$ fm). Left and right panels correspond, respectively, to the x and y axis in the transverse plane $z = 0$. Solid and dashed lines are calculated with EoS-PT and EoS-HG, respectively.

¹²Essentially the same effect is responsible for the broadening of baryon rapidity distribution in central collisions as discussed in Secs. III D and V.

¹³A similar conclusion about the increase of elliptic flow due to phase-transition effects at FAIR energies has been made recently in Ref. [58].

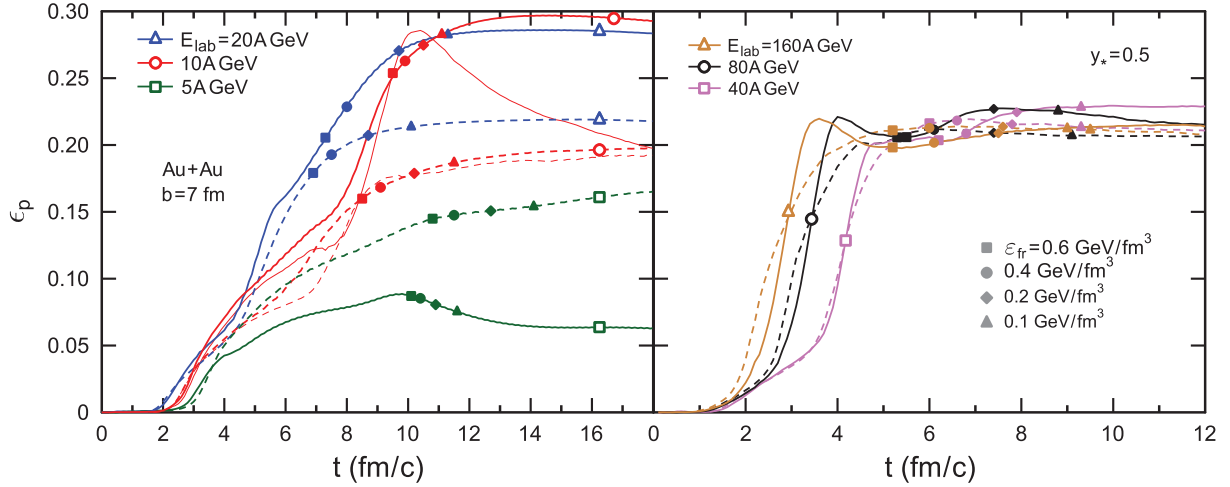


FIG. 19. (Color online) Time dependence of the momentum anisotropy in Au + Au collisions at different bombarding energies ($b = 7$ fm). The solid (dashed) lines correspond to EoS-PT (EoS-HG). Full symbols on the curves mark freeze-out times corresponding to different ε_{fr} indicated in the right panel. Open symbols mark the bombarding energy values. Thin lines in the left panel show the results of calculations for $E_{\text{lab}} = 10$ GeV/nucleon with a simplified definition of ε_p (see text).

heavy-ion collisions. To estimate a possible spread of results, we determine the time moment t_{fr} when the energy density in a central box becomes smaller at a certain freeze-out value ε_{fr} . Applying such a freeze-out condition, in Fig. 19 we mark by points the values of ε_p corresponding to different values of ε_{fr} . Figure 20 shows excitation functions of the momentum anisotropy for two EoSs. The lines connect the values of ε_p taken at $t = t_{\text{fr}}$, where t_{fr} corresponds to $\varepsilon_{\text{fr}} = 0.4$ GeV/fm³. At each E_{lab} the ends of arrows in Fig. 20 show the values of ε_p for $\varepsilon_{\text{fr}} = 0.2$ and 0.6 GeV/fm³. In the case

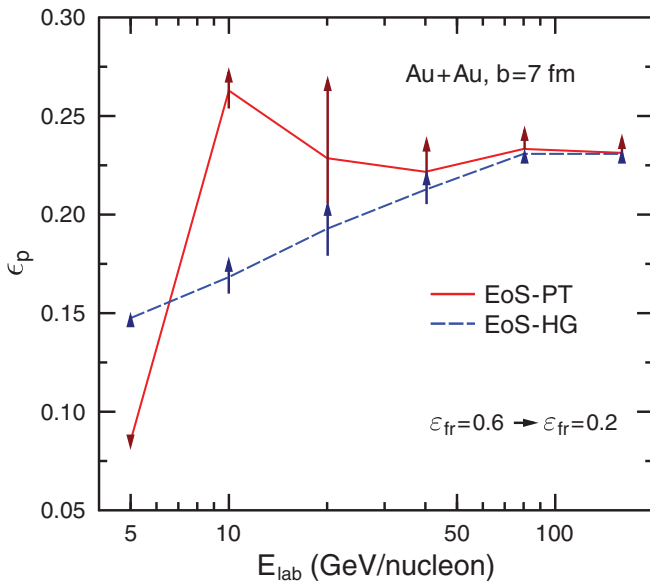


FIG. 20. (Color online) Excitation function of momentum anisotropy in Au + Au collisions with $b = 7$ fm. The solid (dashed) lines correspond to EoS-PT (EoS-HG). Arrows show possible shifts of ε_p values for different choices of freeze-out energy density ε_{fr} between 0.2 and 0.6 GeV/fm³.

of EoS-PT our model predicts a nonmonotonic dependence $\varepsilon_p(E_{\text{lab}})$ with maximum at $E_{\text{lab}} \simeq 10$ GeV/nucleon.

As indicated above, the momentum anisotropy is approximately proportional to the pion elliptic flow at midrapidity. It is interesting that existing experimental data on the proton and pion elliptic flows in Au + Au and Pb + Pb collisions (see their compilation in Ref. [57]) do not exclude the presence of a local maximum of v_2 at high AGS energies. However, the data at AGS and SPS energies were obtained by using different detectors, centrality cuts, and methods of v_2 determination. It would be highly desirable to perform more detailed measurements of the elliptic flow excitation function in the bombarding energy range 5–50 GeV/nucleon. Hopefully, low-energy RHIC as well as future NICA and FAIR experiments will help in obtaining such data.

V. HADRONIC SPECTRA

In this section we present the model results for proton and pion momentum distributions in central Au + Au collisions at $E_{\text{lab}} \simeq 10$ A GeV. These distributions are calculated by using the Cooper-Frye formula (16) with the isochronous freeze-out hypersurface. The results for the EoS-PT include the excluded volume corrections (see Sect. II E). The proton and π^- distributions are obtained from nucleon and pion spectra by introducing the scaling factors Z/A and $1/3$, respectively. The parameter of freeze-out time t_{fr} is chosen to achieve the best fit of experimental data.¹⁴ Our calculations with the EoS-PT show that the best choice corresponds roughly to the end of the hadronization stage. In this case the thermodynamic parameters of central cells become close to the boundary between the MP and HP (see Figs. 9 and 10).

¹⁴To reduce the influence of isospin effects, we fitted our distributions of “negative” pions to one half of the observed charged pion distributions.

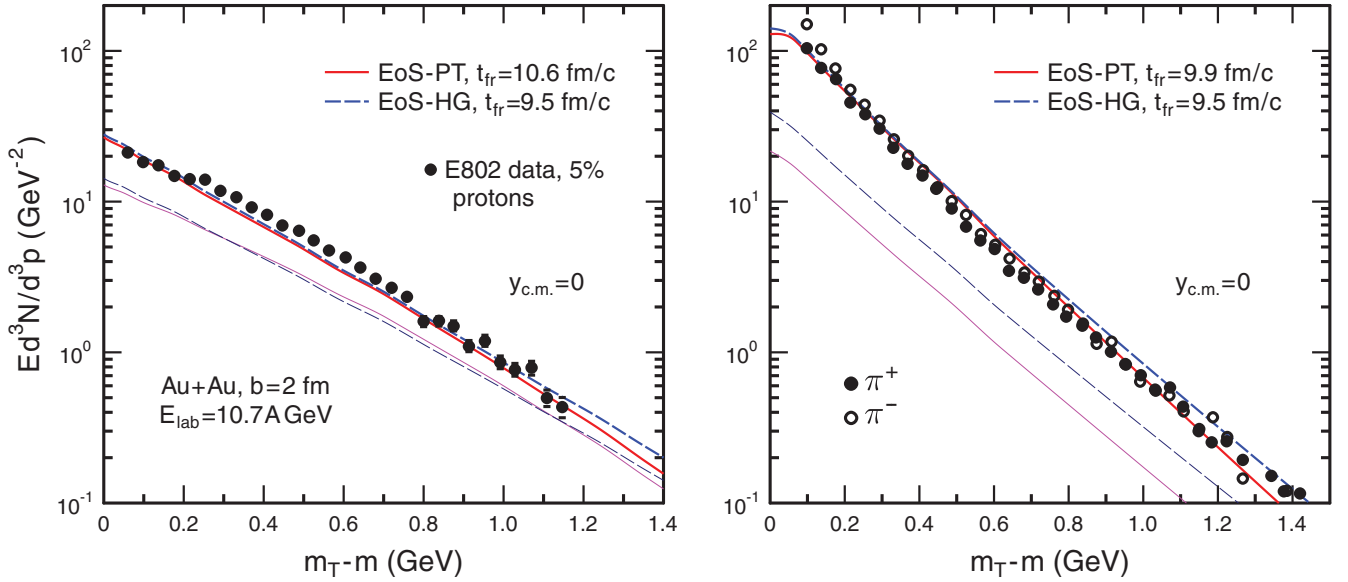


FIG. 21. (Color online) Transverse kinetic energy distributions of protons (left panel) and negative pions (right panel) in 10.7 A GeV Au + Au collision ($b = 2$ fm). Thick solid and dashed lines are calculated with EOS-PT and EOS-HG, respectively. Thin lines show the distributions of thermal hadrons, i.e., without contributions from decays of resonances. Experimental data are taken from [66].

According to our analysis, significant fractions of proton and pion yields in the considered reaction come from decays of resonances. At $E_{\text{lab}} \sim 10$ GeV/nucleon, relative contributions of free (“thermal”) pions and protons at midrapidity are about 25% and 60% of total yields of pions and protons, respectively. Especially important are contributions of isobar decays. This is explained by large values of baryon chemical potential ($\mu \sim 0.6 - 0.7$ GeV at freeze-out) expected in nuclear collisions at AGS and FAIR energies. Keeping in mind that measured

yields include feeding from weak decays of hyperons and K_S^0 mesons, we take into account the corresponding contributions in our calculations.

According to Fig. 21, the proton and pion p_T distributions in central Au + Au collisions at $E_{\text{lab}} \sim 10$ GeV/nucleon are not so sensitive to EoS. In this figure we explicitly show the contributions of thermal proton and pions. One can see that resonance decays give large contributions at all p_T , especially for pions.

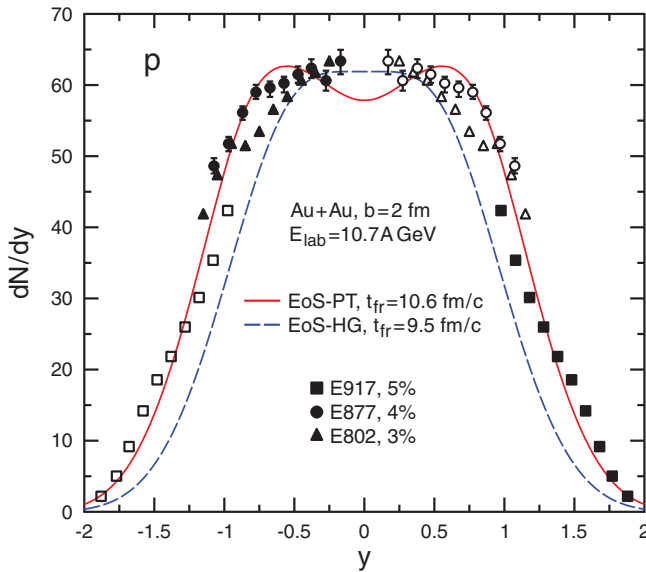


FIG. 22. (Color online) Rapidity distributions of protons in 10.7 A GeV Au + Au collision ($b = 2$ fm). Solid and dashed lines are calculated with EOS-PT and EOS-HG, respectively. Full symbols are experimental data [66–68], and open ones are obtained by reflection with respect to midrapidity.

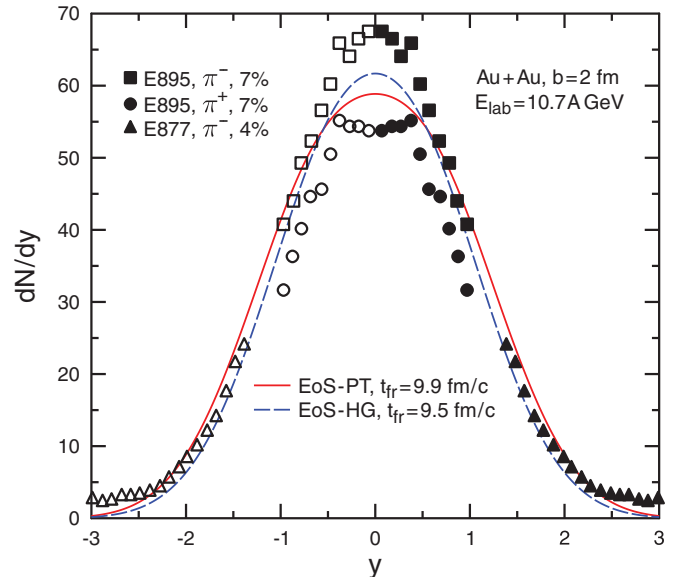


FIG. 23. (Color online) Same as Fig. 22 but for rapidity distributions of π^- mesons. Full symbols are experimental data for charged pions in central Au + Au collisions at $E_{\text{lab}} = 8$ [71] and 9.9 [68] GeV/nucleon. Open symbols are obtained by reflection.

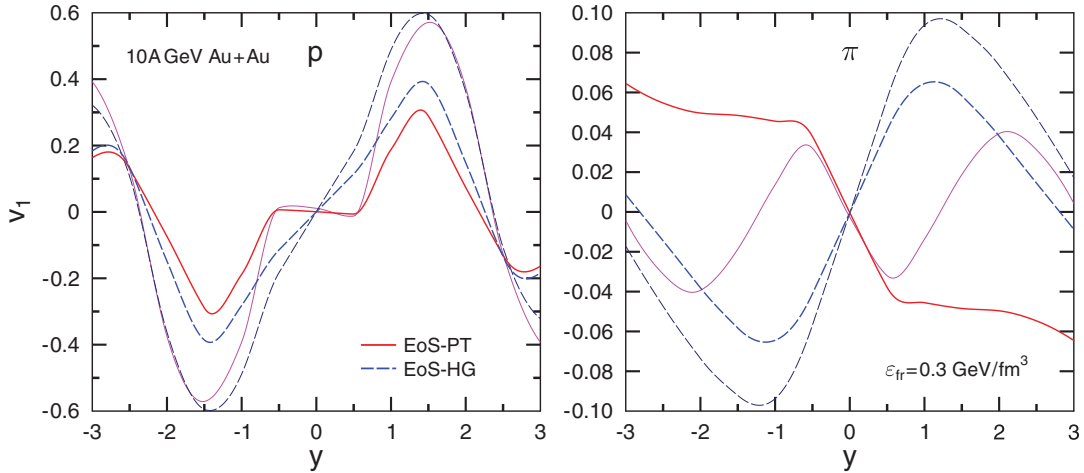


FIG. 24. (Color online) Directed flows of protons (left panel) and charged pions (right panel) as functions of c.m. rapidity in 10 A GeV Au + Au collisions. Solid (dashed) lines are calculated with EoS-PT (EoS-HG). Thick and thin lines correspond to $b = 4$ and 7 fm, respectively.

The proton rapidity distribution for the same reaction is presented in Fig. 22. As compared to the EoS-HG, the calculation with the phase transition predicts a noticeably broader rapidity distribution. In this case the agreement with experimental data outside the central rapidity region is better than in the purely hadronic scenario. The physical meaning for this broadening is related to larger pressure gradients in the longitudinal direction, as demonstrated in Fig. 12. Our analysis shows that the shape of the proton rapidity distribution at small c.m. rapidities is rather sensitive to the excluded volume parameter. It is interesting that single- and three-fluid calculations [69] of central 11 GeV/nucleon

Au + Au collisions also predict appearance of a deep in the proton rapidity distribution at midrapidity for an EoS with the deconfinement phase transition. Irregular behavior of this distribution as a function of bombarding energy has been recently suggested [70] as a signature of the QGP formation.

The π^- rapidity distribution for the 10.7 GeV/nucleon central Au + Au collision is shown in Fig. 23. In the case of the EoS-PT, a reasonable agreement with experimental data can be achieved only if we assume a freeze-out time smaller than for protons.¹⁵ Again, calculations with the phase transition predict a broader distribution than those for the EoS-HG. However, differences in shapes of pion rapidity distributions are not as strong as for protons.

It is worth noting that our results on hadronic spectra and collective flows (see the following section) are rather preliminary. First, they are obtained by using the simplest option of isochronous freeze-out. Second, the resonance decays are considered rather schematically i.e., the width of resonances was neglected and multiparticle decays were included only approximately. Third, in calculating particle spectra we determine local values of temperature and chemical potentials by using linear interpolation of tables prepared with fixed steps in n and ϵ (see Sec. II D). The accuracy of this calculation may be increased by applying more effective schemes of nonlinear interpolation.

VI. COLLECTIVE FLOWS

The momentum anisotropy considered in Sec. IV B is not measurable directly and can be used only for qualitative analysis of collective flows in nuclear collisions. On the other hand, theoretical and experimental studies of the directed (v_1) and elliptic (v_2) flows became very popular in recent years (see,

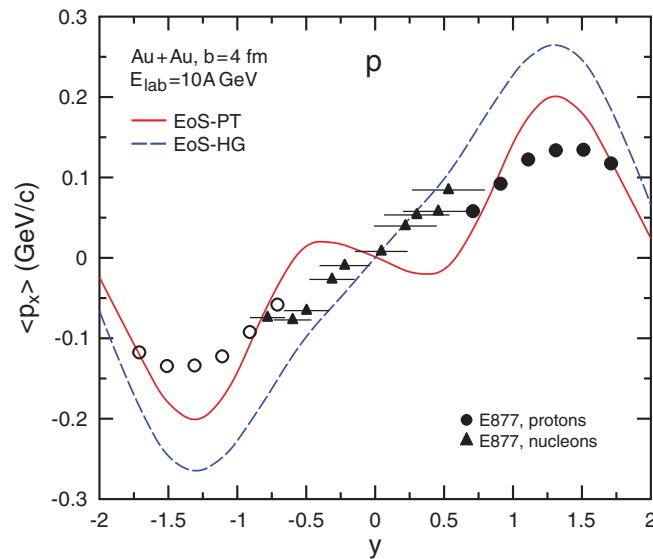


FIG. 25. (Color online) Mean directed transverse momentum of protons as functions of c.m. rapidity in 10 A GeV Au + Au collisions ($b = 4$ fm). Solid and dashed lines are calculated with EoS-PT and EoS-HG, respectively. Experimental data [73] for protons (full dots) and nucleons (full triangles) correspond to 10.1 A GeV midcentral Au + Au collisions. Circles are obtained by reflection.

¹⁵Additional calculations show that freeze-out times for pions and nucleons become closer to each other if one assumes smaller values of excluded volume for thermal pions as compared to nucleons.

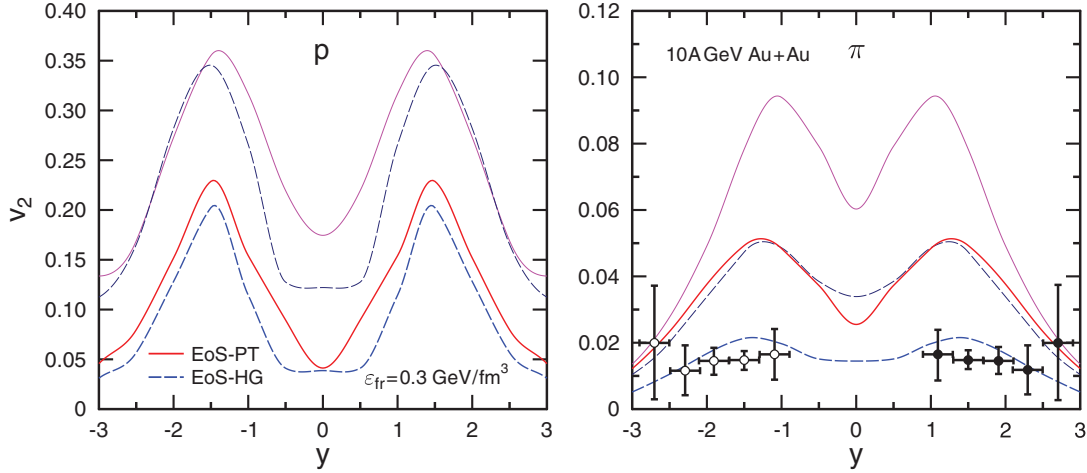


FIG. 26. (Color online) Elliptic flows of protons (left panel) and charged pions (right panel) as functions of rapidity in 10 A GeV Au + Au collisions. Solid (dashed) lines are calculated with EoS-PT (EoS-HG). Thick and thin lines correspond to $b = 4$ and 7 fm, respectively. Full dots are experimental data [75] for negative pions in 10.6 A GeV midcentral Au + Au collisions. Circles are obtained by reflection.

e.g., [72]). In particular, this was initiated by the prediction [34] of a “softest point collapse” of the nucleon-directed flow at $E_{\text{lab}} \sim 8$ GeV/nucleon. In this section we present our results for Au + Au and Pb + Pb collisions at $E_{\text{lab}} = 10$ and 40 GeV/nucleon. These results are obtained by using formulas of Sec. II E.

Figure 24 shows the model predictions for the proton- and pion-directed flows in 10 GeV/nucleon Au + Au collisions. As before, we compare the results obtained for the EoS-PT and EoS-HG. To demonstrate sensitivity to the centrality, we present results for two values of the impact parameter, $b = 4$ and 7 fm. In both cases it is assumed that freeze-out occurs when the energy density in the central cell becomes lower than $\epsilon_{\text{fr}} = 0.3$ GeV/fm³. The model predicts a strong reduction of $|v_1^{(p)}|$ at small $|y|$ in transition from the EoS-HG to EoS-PT.

One can see a noticeable difference of slopes dv_1/dy between two EoSs in a central rapidity region. In addition, negative slopes (antiflow) of the pion and proton v_1 are predicted in the calculation with the EoS-PT. However, this effect is stronger for pions. Our analysis shows that the antiflow in this case is formed mainly due to the contribution of thermal pions. Note that slopes $dv_1^{(\pi)}/dy$ at $|y| \lesssim 0.5$ depend only slightly on b .

Unfortunately, the rapidity dependence of directed flows is not measured at AGS bombarding energies. On the other hand, there are measurements [73] of a similar quantity, the so-called “sideflow” $\langle p_x \rangle$, which is defined as a mean transverse momentum (per particle) projected on the reaction plane. Below we calculate this quantity by using the right-hand side of (19) with the replacement $\cos(2\phi) \rightarrow p_x = p_T \cos \phi$. Figure 25 shows the results for proton and pion sideflows

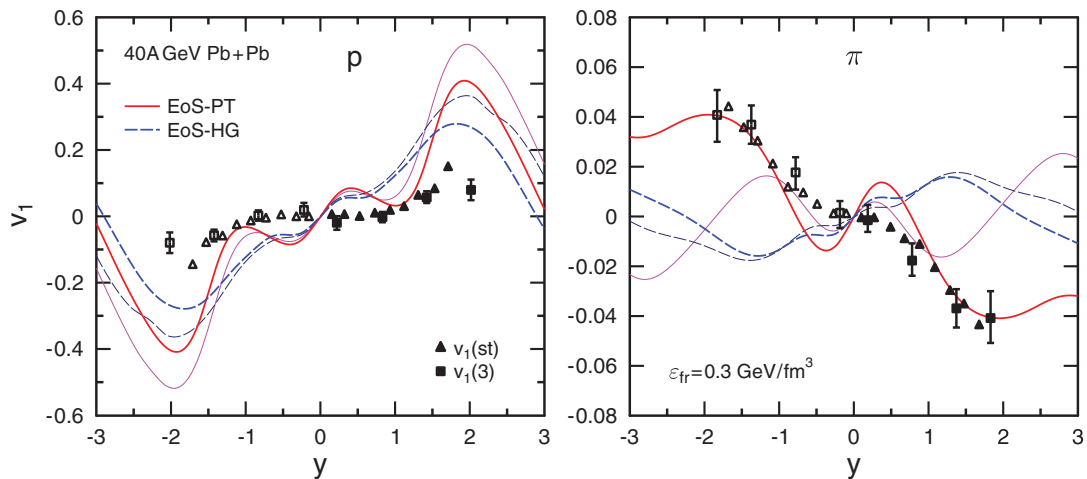


FIG. 27. (Color online) Directed flows of protons (left panel) and charged pions (right panel) as functions of rapidity in 40 A GeV Pb + Pb collisions. Solid (dashed) lines are calculated with EoS-PT (EoS-HG). Thick and thin lines correspond to $b = 4$ and 5.6 fm, respectively. Full symbols are measured experimental data [76], while the open ones are obtained by reflection.

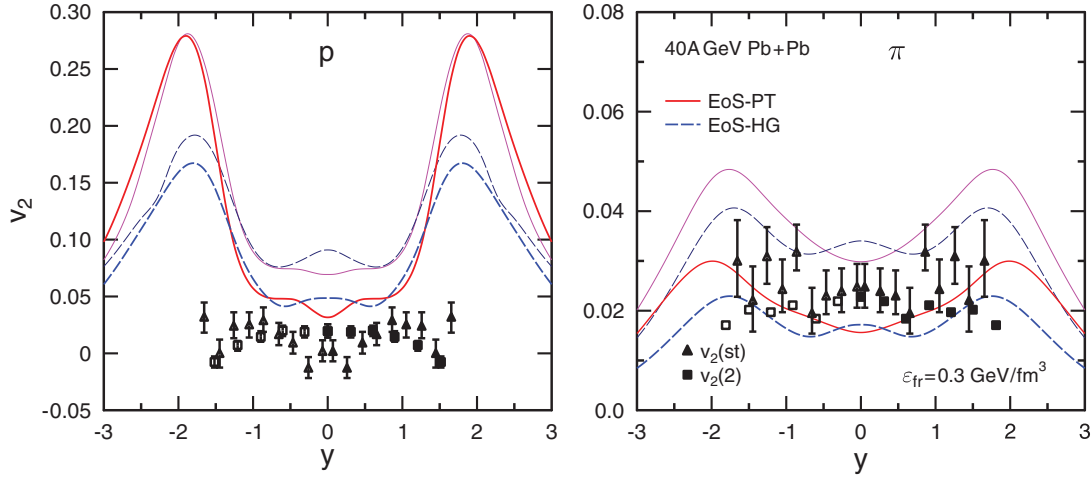


FIG. 28. (Color online) Same as Fig. 27, but for elliptic flows of protons (left panel) and charged pions (right panel).

in 10 GeV/nucleon Au + Au collision with $b = 4$ fm. One can see that the calculation with the EoS-PT predicts a back bending¹⁶ in the central bin, $|y| \lesssim 0.5$, which is not seen in data. On the other hand, the observed maxima of $|\langle p_x \rangle|$ are strongly overestimated in the hadronic scenario.

Figure 26 represents proton and charged pion elliptic flows for the same reaction as in Figs. 24 and 25. In agreement with discussion in Sec. IV B, the deconfinement phase transition leads to enhancement of elliptic flows as compared to the purely hadronic scenario. The relative increase of v_2 is larger for pions. As before, we consider two values of the impact parameter, $b = 4$ and 7 fm. Experimental data exist only for $v_2^{(\pi)}$. They are better reproduced with the EoS-HG. However, strong sensitivity of results to the choice of centrality and the possible influence of dissipative effects (see below) do not permit drawing a more definite conclusion.

To check the sensitivity of collective flows to the bombarding energy, we have performed calculations for Pb + Pb collisions at $E_{\text{lab}} = 40$ GeV/nucleon. The results are shown in Figs. 27 and 28. As compared to the AGS energy (see Fig. 24), the proton-directed flow is not as sensitive to the EoS, at least in the central rapidity region. As one can see from Fig. 27, the calculations with the EoS-PT again predict formation of the pion antiproton flow. In this case experimental data are in qualitative agreement with our calculation, while the EoS-HG leads to the opposite (positive) slope of the directed flow.

A similar conclusion about smaller sensitivity of collective flows to the phase transition at SPS energies may be drawn from Fig. 28. Here we show the rapidity dependence of proton and pion elliptic flows for 40 GeV/nucleon Pb + Pb collisions. Note that experimental values of v_2 strongly depend on the methods used for their determination. One can see that the

model overestimates the proton data at large c.m. rapidities. As discussed in Ref. [57], more definite conclusions can be made only after dissipative and freeze-out effects are carefully evaluated.

VII. CONCLUSIONS AND OUTLOOK

We have developed a (3+1)-dimensional ideal hydrodynamic model to study heavy-ion collisions in the energy range 1–160 GeV/nucleon. The sensitivity of collective flow observables and particle spectra to the first-order deconfinement phase transition have been investigated. Our analysis shows that maximal values of energy and baryon densities in the central box of the colliding system are significantly larger if this phase transition occurs at some intermediate stage of a heavy-ion collision. As compared with the purely hadronic scenario, the calculations with the deconfinement phase transition predict broadening of proton rapidity distributions, enhancement of elliptic flows, and the appearance of directed antiproton flow in the central rapidity region. It is shown that the collective flow parameters are especially sensitive to EoS at $E_{\text{lab}} \simeq 10$ GeV/nucleon. Our calculations with the EoS-PT predict that at such energies the system spends the longest time in the mixed phase. A similar conclusion that this energy domain is optimal for searching signatures of the deconfinement phase transition in nuclear collisions has been made earlier in Ref. [77].

Our analysis does not allow us to decide which EoS, with or without the phase transition, gives better agreement with experimental data. One should bear in mind that our results are obtained by assuming a rather simple isochronous freeze-out and neglecting dissipative effects. To detect clear signatures of the deconfinement transition in nuclear collisions, new detailed measurements of collective flow observables, especially in the central rapidity region, would be needed in NICA and FAIR experiments. In the future we plan to generalize our model by introducing dissipative terms and a more realistic description of the freeze-out process.

¹⁶Similar conclusions that the phase transition at AGS energies leads to the negative slope of the proton sideflow in a central rapidity region have been made in Refs. [34,69,74]. Note that these earlier results were obtained with neglect of excitation and decays of hadronic resonances.

ACKNOWLEDGMENTS

The authors thank Yu. B. Ivanov for giving the results of the three-fluid model, D.H. Rischke for providing us the one-fluid 3D code, and L. P. Csernai, M. I. Gorenstein, P. Huovinen, H. Niemi, D. Yu. Peressounko, and V. D. Toneev for useful discussions. The computational resources were

provided by the Center for Scientific Computing (Goethe University, Frankfurt am Main) and by the Grid Computing Center (the Kurchatov Institute, Moscow). This work was supported in part by DFG Grant No. 436 RUS 113/957/0-1, the Helmholtz International Center for FAIR (Germany), and Grants No. RFBR 09-02-91331 and No. NSH-7235.2010.2 (Russia).

-
- [1] A. Bazavov *et al.*, *Phys. Rev. D* **80**, 014504 (2009).
 [2] Y. Aoki *et al.*, *J. High Energy Phys.* **06** (2009) 088; S. Borsányi *et al.*, *ibid.* **09** (2010) 073.
 [3] J. Adams *et al.* (STAR Collaboration), *Nucl. Phys. A* **757**, 192 (2005); K. Adcox *et al.* (PHENIX Collaboration), *ibid.* **757**, 184 (2005); B. B. Back *et al.* (PHOBOS Collaboration), *ibid.* **757**, 28 (2005).
 [4] M. G. Alford, K. Rajagopal, and F. Wilczek, *Phys. Lett. B* **422**, 247 (1998).
 [5] O. Scavenius, A. Mocsy, I. N. Mishustin, and D. H. Rischke, *Phys. Rev. C* **64**, 045202 (2001).
 [6] M. A. Stephanov, *Prog. Theor. Phys. Suppl.* **153**, 139 (2004); M. A. Stephanov, *Int. J. Mod. Phys. A* **20**, 4387 (2005).
 [7] H. G. Ritter, *PoS CPOD2006*, 015 (2006); G. Odyniec, *J. Phys. G: Nucl. Part. Phys.* **37**, 094028 (2010).
 [8] NICA white paper [<http://theor.jinr.ru/twiki/cgi/view/NICA/NICAWhitePaper>].
 [9] [FAIR] An International Accelerator Facility for Beams of Ions and Antiprotons, Conceptual Design Report [<http://www.gsi.de/GSI-Future/cdr/>].
 [10] L. D. Landau, *Izv. Akad. Nauk, Ser. Fiz.* **17**, 51 (1953); in *Collected Papers of L. D. Landau* (Gordon and Breach, New York, 1965), p. 665.
 [11] J. D. Bjorken, *Phys. Rev. D* **27**, 140 (1983).
 [12] I. N. Mishustin and L. M. Satarov, *Sov. J. Nucl. Phys.* **37**, 532 (1983).
 [13] J. P. Blaizot and J. Y. Ollitrault, *Phys. Rev. D* **36**, 916 (1987).
 [14] K. J. Eskola, K. Kajantie, and P. V. Ruuskanen, *Eur. Phys. J. C* **1**, 627 (1998).
 [15] B. Mohanty and J. Alam, *Phys. Rev. C* **68**, 064903 (2003).
 [16] L. M. Satarov, I. N. Mishustin, A. V. Merdeev, and H. Stöcker, *Phys. Rev. C* **75**, 024903 (2007); A. V. Merdeev, and H. Stöcker, *Phys. At. Nucl.* **70**, 1773 (2007).
 [17] P. F. Kolb, J. Sollfrank, and U. Heinz, *Phys. Lett. B* **459**, 667 (1999).
 [18] S. A. Bass and A. Dumitru, *Phys. Rev. C* **61**, 064909 (2000).
 [19] D. Yu. Peressounko and Yu. E. Pokrovsky, *Nucl. Phys. A* **669**, 196 (2000).
 [20] D. Teaney, J. Lauret, and E. V. Shuryak, *Phys. Rev. Lett.* **86**, 4783 (2001); [arXiv:nucl-th/0110037](https://arxiv.org/abs/nucl-th/0110037).
 [21] J. Sollfrank, P. Huovinen, M. Kataja, P. V. Ruuskanen, M. Prakash, and N. R. Venugopala, *Phys. Rev. C* **55**, 392 (1997).
 [22] C. Nonaka, E. Honda, and S. Muroya, *Eur. J. Phys. C* **17**, 663 (2000).
 [23] C. E. Aguiar, Y. Hama, T. Kodama, and T. Osada, *Nucl. Phys. A* **698**, 639 (2002).
 [24] T. Hirano and K. Tsuda, *Phys. Rev. C* **66**, 054905 (2002).
 [25] B. Bäuchle *et al.*, *J. Phys. G* **34**, S1077 (2007).
 [26] P. Bozek and I. Wykiel, *Phys. Rev. C* **79**, 044916 (2009).
 [27] B. Schenke, S. Jeon, and C. Gale, *Phys. Rev. C* **82**, 014903 (2010).
 [28] H. Song and U. Heinz, *Phys. Rev. C* **77**, 064901 (2008).
 [29] M. Luzum and P. Romatschke, *Phys. Rev. C* **78**, 034915 (2008); M. Luzum and P. Romatschke, *ibid.* **79**, 039903(E) (2009).
 [30] A. A. Amsden, G. F. Bertsch, F. H. Harlow, and J. R. Nix, *Phys. Rev. Lett.* **35**, 905 (1975).
 [31] H. Stöcker, J. A. Maruhn, and W. Greiner, *Z. Phys. A* **290**, 297 (1979).
 [32] A. S. Roshal and V. N. Russkikh, *Sov. J. Nucl. Phys.* **33**, 817 (1982).
 [33] L. Bravina, L. P. Csernai, P. Lévai, and D. Strottman, *Phys. Rev. C* **50**, 2161 (1994).
 [34] D. H. Rischke, Y. Pürsün, J. A. Maruhn, H. Stöcker, and W. Greiner, *Heavy Ion Phys.* **1**, 309 (1995).
 [35] K. Paech, M. Reiter, A. Dumitru, H. Stöcker, and W. Greiner, *Nucl. Phys. A* **681**, 41c (2001).
 [36] A. A. Amsden, A. S. Goldhaber, F. H. Harlow, and J. R. Nix, *Phys. Rev. C* **17**, 2080 (1978).
 [37] R. B. Clare and D. Strottman, *Phys. Rep.* **141**, 178 (1986).
 [38] I. N. Mishustin, V. N. Russkikh, and L. M. Satarov, *Sov. J. Nucl. Phys.* **48**, 454 (1988); *Nucl. Phys. A* **494**, 595 (1989).
 [39] U. Katscher, D. H. Rischke, J. A. Maruhn, W. Greiner, I. N. Mishustin, and L. M. Satarov, *Z. Phys. A* **346**, 209 (1993).
 [40] J. Brachmann *et al.*, *Phys. Rev. C* **61**, 024909 (2000).
 [41] Yu. B. Ivanov, V. N. Russkikh, and V. D. Toneev, *Phys. Rev. C* **73**, 044904 (2006).
 [42] F. Cooper and G. Frye, *Phys. Rev. D* **10**, 186 (1974).
 [43] K. Bugaev, *Nucl. Phys. A* **606**, 559 (1996).
 [44] C. M. Hung and E. Shuryak, *Phys. Rev. C* **57**, 1891 (1998).
 [45] C. Nonaka and S. A. Bass, *Phys. Rev. C* **75**, 014902 (2007).
 [46] T. Hirano, U. W. Heinz, D. Kharzeev, R. Lacey, and Y. Nara, *Phys. Rev. C* **77**, 044909 (2008).
 [47] H. Petersen, J. Steinheimer, G. Berau, M. Bleicher, and H. Stöcker, *Phys. Rev. C* **78**, 044901 (2008).
 [48] L. M. Satarov, M. N. Dmitriev, and I. N. Mishustin, *Phys. Atom. Nucl.* **72**, 1390 (2009).
 [49] L. D. Landau and E. M. Lifshitz, *Fluid Mechanics* (Pergamon Press, New York, 1987).
 [50] J. P. Boris and D. L. Book, *J. Comput. Phys.* **11**, 38 (1973).
 [51] D. H. Rischke, S. Bernard, and J. A. Maruhn, *Nucl. Phys. A* **595**, 346 (1995).
 [52] L. D. Landau and E. M. Lifshitz, *Statistical Physics* (Pergamon Press, New York, 1980).
 [53] D. H. Rischke, M. I. Gorenstein, H. Stöcker, and W. Greiner, *Z. Phys. C* **51**, 485 (1991).
 [54] K. Nakamura *et al.* (Particle Data Group), *J. Phys. G* **37**, 075021 (2010).
 [55] J.-Y. Ollitrault, *Phys. Rev. D* **46**, 229 (1992).
 [56] P. F. Kolb, J. Sollfrank, and U. Heinz, *Phys. Rev. C* **62**, 054909 (2000).
 [57] Yu. B. Ivanov, I. N. Mishustin, V. N. Russkikh, and L. M. Satarov, *Phys. Rev. C* **80**, 064904 (2009).
 [58] H. Petersen and M. Bleicher, *Phys. Rev. C* **81**, 044906 (2010).

- [59] I. N. Mishustin, V. N. Russkikh, and L. M. Satarov, *Sov. J. Nucl. Phys.* **54**, 260 (1991).
- [60] P. Bozek, *Phys. Rev. C* **79**, 054901 (2009).
- [61] Ya. B. Zeldovich and Yu. P. Raizer, *Physics of Shock Waves and High-Temperature Hydrodynamic Phenomena* (Academic Press, New York, 1967).
- [62] V. M. Galitsky and I. N. Mishustin, *Phys. Lett. B* **72**, 285 (1978).
- [63] L. P. Csernai, *Introduction to Relativistic Heavy Ion Collisions* (Wiley & Sons, New York, 1994).
- [64] Yu. B. Ivanov (private communication).
- [65] V. D. Toneev *et al.*, *Eur. Phys. J. C* **32**, 399 (2004).
- [66] L. Ahle *et al.* (E802 Collaboration), *Phys. Rev. C* **57**, R466 (1998).
- [67] B. B. Back *et al.* (E917 Collaboration), *Phys. Rev. Lett.* **86**, 1970 (2001).
- [68] J. Barrette *et al.* (E877 Collaboration), *Phys. Rev. C* **62**, 024901 (2000).
- [69] J. Brachmann, A. Dumitru, J. A. Maruhn, H. Stöcker, W. Greiner, and D. H. Rischke, *Nucl. Phys. A* **616**, 391 (1997).
- [70] Yu. B. Ivanov, *Phys. Lett. B* **690**, 358 (2010).
- [71] J. L. Klay *et al.* (E895 Collaboration), *Phys. Rev. C* **68**, 054905 (2003).
- [72] H. Stöcker, *Nucl. Phys. A* **750**, 121 (2005).
- [73] J. Barrette *et al.* (E877 Collaboration), *Phys. Rev. C* **56**, 3254 (1997).
- [74] L. P. Csernai and D. Röhrich, *Phys. Lett. B* **458**, 454 (1999).
- [75] K. Filimonov *et al.* (E877 Collaboration), *Nucl. Phys. A* **661**, 198 (1999).
- [76] C. Alt *et al.* (NA49 Collaboration), *Phys. Rev. C* **68**, 034903 (2003).
- [77] I. C. Arsene *et al.*, *Phys. Rev. C* **75**, 034902 (2007).